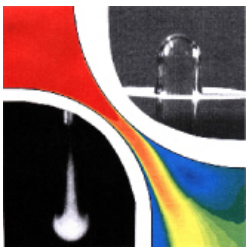

Christoph Irrenfried

Direct numerical simulation of turbulent heated pipe flow at high Prandtl numbers

Master Thesis

Graz University of Technology

Institute for Fluid Mechanics and Heat Transfer
Head: Univ.-Prof. Dr.-Ing. habil. Brenn

Supervisor: Ao.Univ.-Prof. Dipl-Ing. Dr.techn. Steiner

Graz, November 2013

This document is set in Palatino, compiled with pdfLaTeX2e and `Biber`.

The LaTeX template from Karl Voit is based on KOMA script and can be found online: https://github.com/novoid/LaTeX-KOMA-template

Statutory Declaration

I declare that I have authored this thesis independently, that I have not used other than the declared sources/resources, and that I have explicitly marked all material which has been quoted either literally or by content from the used sources.

Graz, _____ _____

Date Signature

Eidesstattliche Erklärung[1]

Ich erkläre an Eides statt, dass ich die vorliegende Arbeit selbstständig verfasst, andere als die angegebenen Quellen/Hilfsmittel nicht benutzt, und die den benutzten Quellen wörtlich und inhaltlich entnommenen Stellen als solche kenntlich gemacht habe.

Graz, am _____ _____

Datum Unterschrift

[1] Beschluss der Curricula-Kommission für Bachelor-, Master- und Diplomstudien vom 10.11.2008; Genehmigung des Senates am 1.12.2008

Acknowledgement

First of all, I would like to express my gratitude to my supervisor Prof. Steiner for the continuous support and guidance.

Furthermore, I'm very grateful for the advice and support of the entire staff of the Institute of Fluid Mechanics.

Most importantly, I would like to give special thank to my friends and family, who have supported me throughout the entire studies. It would not have been possible without them.

Abstract

The numerical simulation of turbulent heat transfer at high molecular Prandtls number is still strongly challenged by disparate thicknesses of the viscous sublayers for the velocity and the temperature. The modelling assumptions generally made for the prescription of the thermal boundary conditions in $RANS$-type simulations become increasingly questionable for higher Prandtl numbers. The present work addresses this issue performing Direct Numerical Simulations of turbulent heated pipe flow varying the molecular Prandtl number from $Pr = 1$ to $Pr = 10$. The DNS results basically confirm the major model assumptions in that the turbulent Prandtl number Pr_T and the von Kármán constant κ remain on the same constant levels inside the inertial sublayer for all considered Prandtl numbers. However, these assumptions break down in the viscous sublayer, where the turbulent Prandtl number is strongly increased for the higher Pr. Nonetheless, the P-function proposed by Jayatilleke (1969) in order to model the thermal resistance of the viscous sublayer still shows good agreement with the corresponding DNS data. The validation against the DNS results further demonstrates that any reliable wall-function, i. e. log-law, based modelling of the thermal boundary conditions most importantly requires an appropriate prescription of the thermal mixing length $l^+_{m\theta} = \kappa_\theta y^+$ in terms of the suitable setting for $\kappa_\theta = \frac{\kappa}{Pr_T}$ determining the linear increase with the wall distance y^+.

Nomenclature and Abbreviations

Roman symbols

Symbol	Description	Dimension
a	thermal diffusivity	m^2/s
a_T	eddy conductivity	m^2/s
c_f	local friction coefficient	$-$
c_p	specific heat at constant pressure	J/kgK
c_v	specific heat at constant volume	J/kgK
D	diameter	m
e	specific internal energy	J/kg
Ec	Eckert number	$-$
L	length of pipe	m
l_m	mixing length	m
$l^+_{m\theta}$	thermal mixing length	m
Nu	Nusselt number	$-$
Nu_D	Nusselt number	$-$
p	pressure	Pa
Pe	Peclet number	$-$
Pe_T	turbulent Peclet number	$-$
Pr	Prandtl number	$-$
Pr_T	turbulent Prandtl number	$-$
$\underline{q}$	heat flux	W/m^2
$\dot{q}_Q$	internal heat source	W/m^3
q_w	wall heat flux	W/m^2
$\dot{Q}$	heat flux	W
R	radius	m

Symbol	Description	Dimension
Re_D	Reynolds number	$-$
Re_τ	Reynolds number	$-$
r	radial direction	m
t	time	s
T	temperature	K
T_τ	friction temperature	K
T_w	wall temperature	K
$\underline{u}$	velocity	m/s
u_i, U, V, W	velocity component	m/s
w_τ	friction velocity	m/s
y	wall-normal direction	m
z	axial direction	m

Greek Symbols

Symbol	Description	Dimension
α	heat transfer coefficient	W/m^2K
δ	velocity boundary-layer thickness	m
δ_T	thermal boundary-layer thickness	m
κ	von Kármán constant	$-$
λ	thermal conductivity	W/mK
μ	dynamic viscosity	kg/ms
ν	kinematic viscosity	m^2/s
ν_T	eddy diffusivity for momentum transfer	m^2/s
ϕ	azimuthal direction	$-$
ρ	density	kg/m^3
$\underline{\underline{\tau}}$	stress tensor	N/m^2
τ_w	wall shear stress	N/m^2

Symbol	Description	Dimension
Θ	transformed temperature	K
ϑ	observation period	s

Subscripts

Symbol	Description
$()^*$	non-dimensionalized
$()^+$	representation in wall-coordinates
$()'$	fuctuation component
$\overline{()}$	statistical average
$()_m$	bulk mean value

Abbreviations

DNS	Direct numerical simulation
LES	Large eddy simulation
CFD	Computational fluid dynamics
RANS	Reynolds Averaged Navier-Stokes equations
MPI	Message Passing Interface
CFL	Courant–Friedrichs–Lewy condition
rms	Root mean square

Contents

List of Figures

1 Introduction

In mechanical engineering heat transfer into a pipe flow is of high importance, as it is met in a wide field of technical applications. Flows with high Prandtl numbers are of special interest, when dealing with operating fluids like organic cooling liquids, or oils. In figure 1.1, the range of Prandtl numbers is shown for different fluids. The reliable modelling of the turbulent convective heat transfer into these liquids is still a very challenging task. In this thesis, special attention was given to the Prandtl numbers 1.0, 2.0, 5.9 (water), and 10 (the lower limit of the oil range).

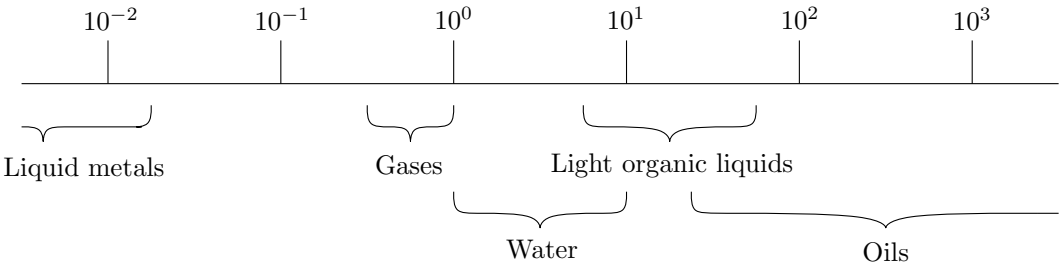

Figure 1.1: Range of Prandtl numbers.

In a pipe flow, the most interesting region is the near-wall zone, where the flow is highly affected by viscous forces, so that the flow structures differ significantly from those in the turbulent core region. The numerical resolution of small scale structures occurring in this near-wall layer requires a strongly refined computational grid, which would mostly lead to unacceptably high computational costs. For this reason, most of the currently available Computational Fluid Dynamics (CFD) codes are working with wall models. The significant advantage of such models is that only the core

region of the flow is simulated, while the near wall region is described using analytical wall functions, which reduces the computational costs markedly. Most of the analytical functions developed for the near-wall temperature introduce the turbulent Prandtl number as important model parameter. To reduce the complexity of the model most simulation codes use constant values for this parameter, although it may considerably increase towards the wall, as it is shown in Kays and Crawford (1993).

The present thesis computationally investigates the accuracy of the most popular wall function based concepts for modelling the turbulent wall heat transfer with a particular focus on cases with higher Prandtl numbers. For this purpose, a turbulent pipe flow with a Reynolds number of $Re_D = 5300$ ($Re_\tau = 360$) and a constant wall heat flux was considered.
The computational description of the convective wall heat transfer typically faces the problem, that for increasing Prandtl numbers, the thickness of the thermal boundary layer decreases in comparison to the velocity boundary layer, which means that the essential transport mechanisms for heat occur closer and closer to the wall. Therefore, the modelling in this area becomes more important as the Prandtl number increases. The evaluation of any model approach requires a very comprehensive and realistic description of the conditions near the wall, which must not neglect any physically relevant effect. This requires a high level of accuracy, which can only be provided by a direct numerical simulation (DNS).

The majority of previous studies performing direct numerical simulations of heated channel flows, considered fairly low Prandtl numbers. One of the first attempts were made by Kim and Moin (1987), who examined only flows with Prandtl numbers less than two. In a later study, Antonia and Kim (1991) found a simple correlation for the spatial distribution of turbulent Prandtl number Pr_T based on a DNS simulation applying numerous simplifying assumptions. A more recent DNS study of a plane channel flow including an evaluation of Pr_T was done by Kawamura et al. (1999). However, these simulations were performed at Prandtl numbers less than 1, which has the advantage that the thermal boundary layer is thicker than the velocity boundary layer, so that the computational grid does not have to be additionally refined to resolve the heat transfer near the wall.

Besides the DNS investigations, large eddy simulation techniques (LES) were used to investigate heat transfer into pipe flows. Solving for spatially filtered transport equation LES captures directly only the large scale structures while it models all small scale phenomena, rather than resolving them like in a DNS. Therefore, the number of grid cells can be reduced, which reduces the computation time. A recent study done by Ould-Rouiss et al. (2013) investigated the influence of a high Prandtl number ($Pr >= 7$) and a high Reynolds number ($Re_D >= 20000$) on a heated pipe flow.

The very thin thermal boundary layers met at high Prandtl numbers pose also a great difficulty to experimental investigations. It is a very challenging task to measure accurately the turbulent fluxes and temperature gradient next to the wall. Therefore, reliable experimental data for the variation of the turbulent Prandtl number close to the wall are hardly available. One of the few measurements involving a high Prandtl number flow, was performed by Hollingsworth et al. (1989) considering a turbulent thermal boundary layer along a flat-plate with zero-pressure-gradient.
The still limited insight into the detailed conditions near the heated wall provided thus far by experiments and numerical simulations motivated to perform the DNS based investigation in the present work. The maximum considered Prandtl number was $Pr = 10$, which was associated with extremely high but still affordable computational costs.

2 Fundamentals

2.1 Transport equations

The computational investigation of heated or cooled flow problems has basically to solve the conservation equations of mass, momentum and energy. The balance equations for mass and momentum are the so called Navier-Stokes equations, which can be written in a conservative vectorial formulation as

$$\frac{\partial \rho}{\partial t} + \underline{\nabla} \cdot (\rho \underline{u}) = 0 \tag{2.1}$$

$$\frac{\partial \rho \underline{u}}{\partial t} + \underbrace{\underline{\nabla} \cdot (\rho \underline{u}\, \underline{u})}_{\underline{A} \text{ ... advection}} = -\underline{\nabla} P + \underbrace{\underline{\nabla} \cdot \underline{\underline{\tau}}}_{\underline{D} \text{ ... diffusion}} . \tag{2.2}$$

The conservation equation of energy reads

$$\frac{\partial \rho e}{\partial t} + \underline{\nabla} \cdot (\rho \underline{u} e) = -p \underline{\nabla} \cdot \underline{u} + \underline{\underline{\tau}} : \underline{\nabla}\, \underline{u} - \underline{\nabla} \cdot \underline{q} + \dot{q}_Q. \tag{2.3}$$

The computational investigation in this thesis considers a pressure driven, incompressible, fully developed, turbulent circular pipe flow. For such an axisymmetric wall-bounded flow problem, it is convenient to rewrite the Navier-Stokes equations in cylindrical coordinates as follows:

- continuity equation

$$\frac{1}{r}\frac{\partial(rU)}{\partial r} + \frac{1}{r}\frac{\partial V}{\partial \phi} + \frac{\partial W}{\partial z} = 0 \tag{2.4}$$

- momentum equation into the radial direction

$$\begin{aligned}\frac{\partial U}{\partial t} + \underbrace{\frac{1}{r}\frac{\partial(rUU)}{\partial r} + \frac{1}{r}\frac{\partial(UV)}{\partial \phi} - \frac{V^2}{r} + \frac{\partial(UW)}{\partial z}}_{\text{advection term = inertial forces}} = \\ -\frac{\partial P}{\partial r} + \underbrace{\left[\frac{1}{r}\frac{\partial(r\tau_{rr})}{\partial r} + \frac{1}{r}\frac{\partial \tau_{r\phi}}{\partial \phi} + \frac{\tau_{\phi\phi}}{r} + \frac{\partial \tau_{rz}}{\partial z}\right]}_{\text{diffusion term = viscous forces}}\end{aligned} \tag{2.5}$$

- momentum equation into the azimutal direction

$$\begin{aligned}\frac{\partial V}{\partial t} + \underbrace{\frac{1}{r}\frac{\partial(rVU)}{\partial r} + \frac{1}{r}\frac{\partial(VV)}{\partial \phi} + \frac{VU}{r} + \frac{\partial(VW)}{\partial z}}_{\text{advection term = inertial forces}} = \\ -\frac{1}{r}\frac{\partial P}{\partial \phi} + \underbrace{\left[\frac{1}{r}\frac{\partial(r\tau_{\phi r})}{\partial r} + \frac{\tau_{\phi r}}{r} + \frac{1}{r}\frac{\partial \tau_{\phi\phi}}{\partial \phi} + \frac{\partial \tau_{\phi z}}{\partial z}\right]}_{\text{diffusion term = viscous forces}}\end{aligned} \tag{2.6}$$

- momentum equation into the axial direction

$$\begin{aligned}\frac{\partial W}{\partial t} + \underbrace{\frac{1}{r}\frac{\partial(rWU)}{\partial r} + \frac{1}{r}\frac{\partial(WV)}{\partial \phi} + \frac{\partial(WW)}{\partial z}}_{\text{advection term = inertial forces}} = \\ -\frac{\partial P}{\partial z} + \underbrace{\left[\frac{1}{r}\frac{\partial(r\tau_{zr})}{\partial r} + \frac{1}{r}\frac{\partial \tau_{z\phi}}{\partial \phi} + \frac{\partial \tau_{zz}}{\partial z}\right]}_{\text{diffusion term = viscous forces}}\end{aligned} \tag{2.7}$$

Assuming a Newtonian-fluid, the viscous stresses are written as

$$\tau_{rr} = 2\nu \frac{\partial U}{\partial r} \tag{2.8}$$

$$\tau_{\phi\phi} = 2\nu \left(\frac{1}{r}\frac{\partial V}{\partial \phi} + \frac{U}{r} \right) \tag{2.9}$$

$$\tau_{zz} = 2\nu \frac{\partial W}{\partial z} \tag{2.10}$$

$$\tau_{r\phi} = \tau_{\phi r} = \nu \left[r\frac{\partial}{\partial r}\left(\frac{V}{r}\right) + \frac{1}{r}\frac{\partial U}{\partial \phi} \right] \tag{2.11}$$

$$\tau_{\phi z} = \tau_{z\phi} = \nu \left[\frac{\partial V}{\partial z} + \frac{1}{r}\frac{\partial W}{\partial \phi} \right] \tag{2.12}$$

$$\tau_{zr} = \tau_{rz} = \nu \left[\frac{\partial W}{\partial r} + \frac{\partial U}{\partial z} \right]. \tag{2.13}$$

The energy equation (2.3) rewritten in terms of the temperature, using $e = cT$ reads:

$$\begin{aligned} &\frac{\partial T}{\partial t} + \frac{1}{r}\frac{\partial (rUT)}{\partial r} + \frac{1}{r}\frac{\partial (VT)}{\partial \phi} + \frac{\partial (WT)}{\partial z} = \\ &+ \underbrace{\frac{\lambda}{\rho c}}_{a} \left[\frac{1}{r}\frac{\partial}{\partial r}\left(r\frac{\partial T}{\partial r} \right) + \frac{1}{r^2}\frac{\partial^2 T}{\partial \phi^2} + \frac{\partial^2 T}{\partial z^2} \right] \end{aligned} \tag{2.14}$$

Due to the assumption of incompressible flow with constant density the energy equation contains no pressure dilatation term. The effect of viscous dissipation is neglected as well.

2.2 Turbulent flow

A turbulent flow is characterised by irregular and chaotic fluctuations of the flow quantities. Turbulent flow occurs at Reynolds numbers which exceed a certain critical limit. Beyond this critical limit, which depends on the considered flow configuration, the inertial forces dominate over the viscous forces resulting in highly unstable flow conditions. The inertial forces are represented in the momentum equations (2.5) - (2.7) by the nonlinear advective terms on the lefthand side. In the turbulent flow regime the viscous forces represented in equations (2.5) - (2.7) by the diffusive terms on the righthand side are too weak to dampen the fluctuating turbulent motion.

2.2.1 Laminar-turbulent transition

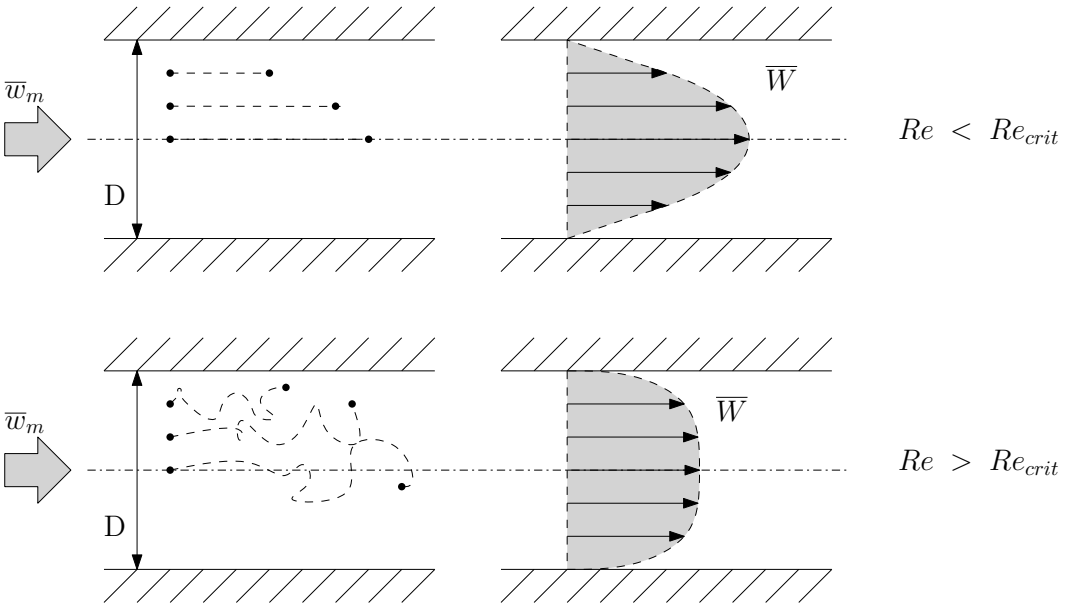

Figure 2.1: Laminar and turbulent pipe flow.

As mentioned above the laminar-turbulent transition depends on the Reynolds number written in the case of a pipe flow as

$$Re_D = \frac{\overline{w}_m D}{\nu}, \tag{2.15}$$

where $\overline{w}_m$ denotes the volumetric flow rate equivalent mean bulk velocity.

If the Reynolds number exceeds a certain value, the critical Reynolds number, the flow becomes unstable. This means that any arbitrarily small perturbation is increased so that the flow finally changes from a laminar into a turbulent state. For example, the critical Reynolds number is around 2300 in the case of cylindrical pipe flow.

In the upper part of figure 2.1, a laminar pipe flow can be seen, where the particle trajectories are parallel to the wall. The lower subfigure shows a typical turbulent state, where the instantaneous velocity components are strongly fluctuating, so that the particles move in a chaotic way. Due to this irregular motion, the pressure drop increases and is roughly proportional to the second power of the bulk velocity in comparison to the laminar flow, where the pressure drop varies linearily with the bulk velocity.

2.2.1.1 Laminar velocity profile

In the laminar flow regime the viscous forces dominate over the inertial forces, so that possible disturbances are always dampened completely, and the flow remains stable. Steady fully developed laminar pipe flows is commonly referred to as ”Hagen-Poiseuille” flow. There is no mass transport into the radial direction, which can be shown by solving the continuity equation (equation (2.4)), imposing no-slip condition at the wall. It then follows from the momentum equation into the radial direction that there is no dependence of the pressure of the radial direction. This implies that the pressure can only vary in the axial direction, i.e.,

$$\frac{\partial p}{\partial r} = 0 \;\Rightarrow\; p \neq f(r),\; p = f(z). \tag{2.16}$$

The laminar streamwise velocity profile is obtained from the solution of the axial momentum equation (equation (2.7)) as

$$w(r) = -\frac{1}{4}\frac{\mathrm{d}p}{\mathrm{d}z}R^2\left(1 - \frac{r^2}{R^2}\right). \tag{2.17}$$

2.2.1.2 Turbulent velocity profile

Figure 2.1 compares a laminar velocity profile against a typical average turbulent velocity profile and example path lines. It can be seen that the turbulent velocity is more bulky, which is caused by the increased momentum transport into the radial direction associated with the turbulent mixing. If the Reynolds number is large enough, Nikuradse found that the law of the wall (commonly termed "log-law", see section 2.4.1) is not only valid in the turbulent near wall region. Accordingly, the "log-law", which is written as

$$\frac{w(r)}{w_{max}} = 1 - \frac{1}{w_{max}}\frac{1}{\kappa}ln\left(\frac{R}{R-r}\right), \tag{2.18}$$

can be also used to describe fairly accurately the core flow region in the center of the pipe.

2.3 Computation of turbulent flow

The majority of technical flow applications are in the turbulent regime. Since turbulent flow is characterized by an unsteady, three-dimensional motion,

all variables vary in all three spatial dimensions and in time. In figure 2.2, a typical fluctuation of a velocity component over the time is shown.

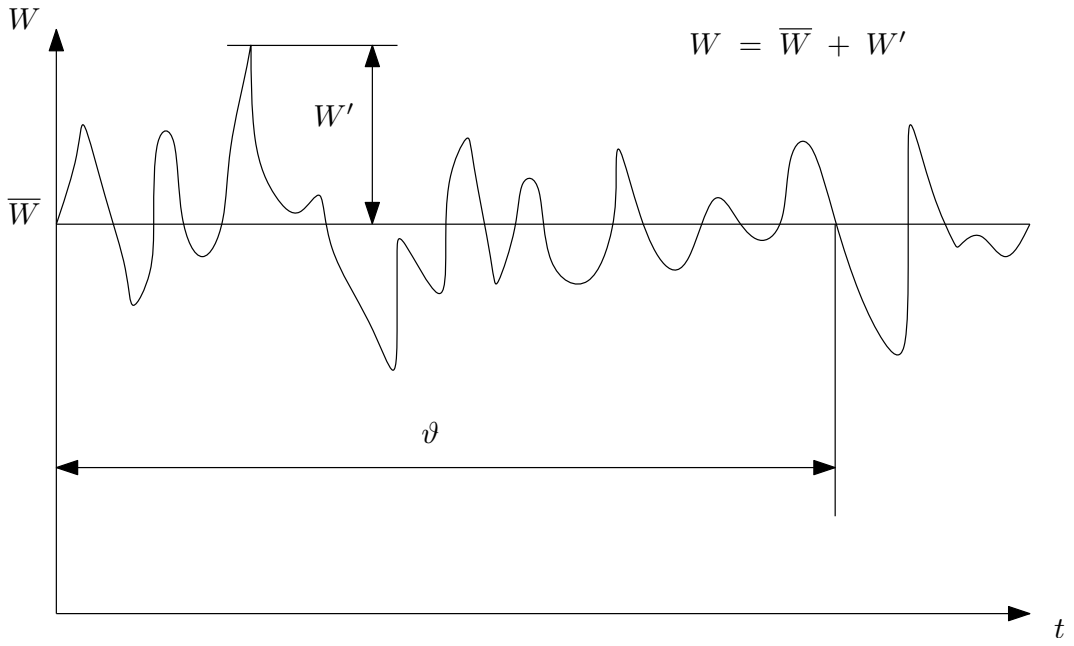

Figure 2.2: RANS approach for the velocity component w.

2.3.1 Direct numerical simulation

The *DNS* approach attempts to calculate the instantaneous values of every flow variable in space and time by solving numerically the governing transport equations, without the assistance of any simplifications or turbulence models. As such it has to resolve the whole range of spatial and temporal scales of turbulence, which requires a very fine computational grid and a small time step size, resulting in large computational meshes and long computation times. Due to the high computational costs the *DNS* is restricted to the computation of generic flow configurations, like turbulent straight channel flows, or turbulent free jets, at fairly low Reynolds numbers. For technically relevant engineering applications, which are mostly associated

with complex geometries and high Reynolds numbers, the concept of DNS is computationally unfeasible. These flows are mostly computed using the "Reynolds Averaged Navier-Stokes" (RANS) approach.

2.3.2 Reynolds Averaged Navier-Stokes (RANS)

The RANS concept is a statistical approach which considers flow variables as statistical random variables varying in space and time. In figure 2.2 the temporal variation of a velocity component is exemplarily shown. The statistics of the flow can be characterised by ensemble averages.

2.3.2.1 Ensemble averages

An ensemble represents the number of realisations of a flow variable in a turbulent flow. In the theoretical limit of an infinite number of realisations, the ensemble average becomes the real statistical average, generally termed Reynolds averaged mean value. Assuming N as number of realisations, the Reynolds averaged mean value of an arbitrary velocity component W_i is defined as

$$\langle W_i \rangle = \lim_{N \to \infty} \frac{1}{N} \sum_{n=1}^{N} W_i^{(n)}$$

Based on this statistical average, Reynolds (1895) proposed to decompose every flow variable into a mean $\langle W_i \rangle$ and a fluctuation w_i written as

$$W_i = \langle W_i \rangle + w_i. \tag{2.19}$$

The standard deviation defined as

$$w_i' = \langle w_i^2 \rangle^{\frac{1}{2}} \tag{2.20}$$

represents the average fluctuation around the mean value.

2.3.2.2 Statistically stationary flow

In the book of Pope (2000) the following definition can be found:

> *A process is statistically stationary, if all multi-time statistics are invariant under a shift in time, i.e., for all positive time intervals ϑ, and all choices of $t_1, t_2, ...t_N$, we have:*
>
> $$f(W_1, t_1 + \vartheta; W_2, t_2 + \vartheta; \ ... \ , W_N, t_N + \vartheta) = f(W_1, t_1; W_2, t_2; \ ... \ , W_N, t_N)$$
>
> *(S.B. Pope, Turbulent flows, 2000)*

Under this conditions the ensemble average obtained in the limit of an infinite number of ensembles does not depend on the time, so that

$$\langle W_i \rangle \neq f(t).$$

It follows that the statistical mean value can be also obtained as temporal average defined as

$$\langle W_i \rangle = \overline{W_i} = \lim_{\vartheta \to \infty} \frac{1}{\vartheta} \int_0^{\vartheta} W_i(t) dt,$$

where ϑ represents the observation time.
In statistically stationary flows the ensemble based Reynolds averaging is evidently equivalent to the time averaging, so that the Reynolds decomposition can be rewritten as

$$
\begin{aligned}
U(r,\phi,z,t) &= \overline{U}(r,\phi,z) + U'(r,\phi,z,t) \\
V(r,\phi,z,t) &= \overline{V}(r,\phi,z) + V'(r,\phi,z,t) \\
W(r,\phi,z,t) &= \overline{W}(r,\phi,z) + W'(r,\phi,z,t) \\
T(r,\phi,z,t) &= \overline{T}(r,\phi,z) + T'(r,\phi,z,t) \\
P(r,\phi,z,t) &= \overline{P}(r,\phi,z) + P'(r,\phi,z,t)
\end{aligned}
$$

where the instantaneous deviations from the temporal means are denoted by the primes.
Introducing this decomposition into the conservation equation for mass, momentum and energy, the so called RANS-type transport equations are obtained. In cylindrical coordinates they read

- continuity equation

$$
\frac{1}{r}\frac{\partial(r\overline{U})}{\partial r} + \frac{1}{r}\frac{\partial\overline{V}}{\partial\phi} + \frac{\partial\overline{W}}{\partial z} = 0 \tag{2.21}
$$

- momentum equation into the radial direction

$$
\begin{aligned}
&\frac{\partial\overline{U}}{\partial t} + \frac{1}{r}\frac{\partial(r\overline{U}\,\overline{U})}{\partial r} + \frac{1}{r}\frac{\partial(\overline{U}\,\overline{V})}{\partial\phi} - \frac{\overline{V}^2}{r} + \frac{\partial(\overline{U}\,\overline{W})}{\partial z} \\
&= -\frac{\partial\overline{P}}{\partial r} + \nu\left[\frac{\partial}{\partial r}\left(\frac{1}{r}\frac{\partial r\overline{U}}{\partial r}\right) + \frac{1}{r^2}\frac{\partial^2\overline{U}}{\partial\phi^2} - \frac{2}{r^2}\frac{\partial\overline{V}}{\partial\phi} + \frac{\partial^2\overline{U}}{\partial z^2}\right] \\
&\quad -\frac{1}{r}\frac{\partial r\overline{U'U'}}{\partial r} - \frac{1}{r}\frac{\partial\overline{U'V'}}{\partial\phi} - \frac{\overline{V'V'}}{r} - \frac{\partial\overline{U'W'}}{\partial z}
\end{aligned} \tag{2.22}
$$

- momentum equation into the azimuthal direction

$$\begin{aligned}
&\frac{\partial \overline{V}}{\partial t} + \frac{1}{r}\frac{\partial (r\overline{V}\,\overline{U})}{\partial r} + \frac{1}{r}\frac{\partial (\overline{V}\,\overline{V})}{\partial \phi} + \frac{\overline{V}\,\overline{U}}{r} + \frac{\partial (\overline{V}\,\overline{W})}{\partial z} \\
&= -\frac{1}{r}\frac{\partial \overline{P}}{\partial \phi} + \nu\left[\frac{\partial}{\partial r}\left(\frac{1}{r}\frac{\partial r\overline{V}}{\partial r}\right) + \frac{1}{r^2}\frac{\partial^2 \overline{V}}{\partial \phi^2} - \frac{2}{r^2}\frac{\partial \overline{U}}{\partial \phi} + \frac{\partial^2 \overline{V}}{\partial z^2}\right] \\
&\quad -\frac{1}{r}\frac{\partial r\overline{V'U'}}{\partial r} - \frac{1}{r}\frac{\partial \overline{V'V'}}{\partial \phi} - \frac{\overline{V'U'}}{r} - \frac{\partial \overline{V'W'}}{\partial z}
\end{aligned} \tag{2.23}$$

- momentum equation into the axial direction

$$\begin{aligned}
&\frac{\partial \overline{W}}{\partial t} + \frac{1}{r}\frac{\partial (r\overline{W}\,\overline{U})}{\partial r} + \frac{1}{r}\frac{\partial (\overline{W}\,\overline{V})}{\partial \phi} + \frac{\partial (\overline{W}\,\overline{W})}{\partial z} \\
&= -\frac{\partial \overline{P}}{\partial z} + \nu\left[\frac{\partial}{\partial r}\left(\frac{1}{r}\frac{\partial r\overline{W}}{\partial r}\right) + \frac{1}{r^2}\frac{\partial^2 \overline{W}}{\partial \phi^2} + \frac{\partial^2 \overline{W}}{\partial z^2}\right] \\
&\quad -\frac{1}{r}\frac{\partial r\overline{W'U'}}{\partial r} - \frac{1}{r}\frac{\partial \overline{W'V'}}{\partial \phi} - \frac{\partial \overline{W'W'}}{\partial z}
\end{aligned} \tag{2.24}$$

- equation of energy

$$\begin{aligned}
&\frac{\partial \overline{T}}{\partial t}\frac{1}{r}\frac{\partial (r\overline{U}\,\overline{T})}{\partial r} + \frac{1}{r}\frac{\partial (\overline{V}\,\overline{T})}{\partial \phi} + \frac{\partial (\overline{T}\,\overline{W})}{\partial z} \\
&= a\left[\frac{1}{r}\frac{\partial}{\partial r}\left(r\frac{\partial \overline{T}}{\partial r}\right) + \frac{1}{r^2}\frac{\partial^2 \overline{T}}{\partial \phi^2} + \frac{\partial^2 \overline{T}}{\partial z^2}\right] \\
&\quad -\frac{1}{r}\frac{\partial r\overline{U'T'}}{\partial r} - \frac{1}{r}\frac{\partial \overline{V'T'}}{\partial \phi} - \frac{\partial \overline{W'T'}}{\partial z}
\end{aligned} \tag{2.25}$$

2.3.2.3 Closure problem

If a three-dimensional problem is considered, there are 14 unknown variables (three mean velocity components, the mean pressure, the mean temperature, and nine turbulent stresses and heat fluxes represented by the non-linear fluctuation terms), but only five equations (continuity, three momentum, and the thermal energy equation) available to solve the problem.

This lack of equations is called ”closure problem”. It is the task of any turbulence model to provide closure for the equation by relating the non-linear turbulent momentum and heat flux terms to the mean values. In channel flows a reliable modelling of these fluxes requires some insight into their behavior near the wall. The main focus of this thesis was on the near wall behaviour of the most relevant turbulent stresses and heat fluxes. The influence of these turbulent fluxes on the momentum and heat transfer inside a turbulent boundary layer will be discussed in the following subsections.

2.4 Turbulent boundary layer

A turbulent flow is generally characterized by a very intense advective transport of momentum, which is represented by the non-linear advection terms on the lefthand side of the Navier-Stokes equations (eq. (2.5) - (2.7)). However, in the proximity of non-moving walls, the flow becomes strongly retarded due to the non-slip condition at the wall, and a velocity boundary layer is formed. Inside the boundary layer the local Reynolds number is strongly reduced with decreasing distance to the wall. This implies that the effect of the viscous stresses is increased, and the effect of the turbulent stresses is decreased, as the wall is approached. Dependent of the contribution of the individual stresses to the total stress balance the structure of the turbulent boundary layer distinguishes several sublayers, as will be shown below.

Assuming the flow as

- fully turbulent
- statistically stationary
- rotationally symmetric

and applying the reductions based on the small thicknesses of the velocity and thermal boundary layers the boundary layer approximation of the RANS equations read

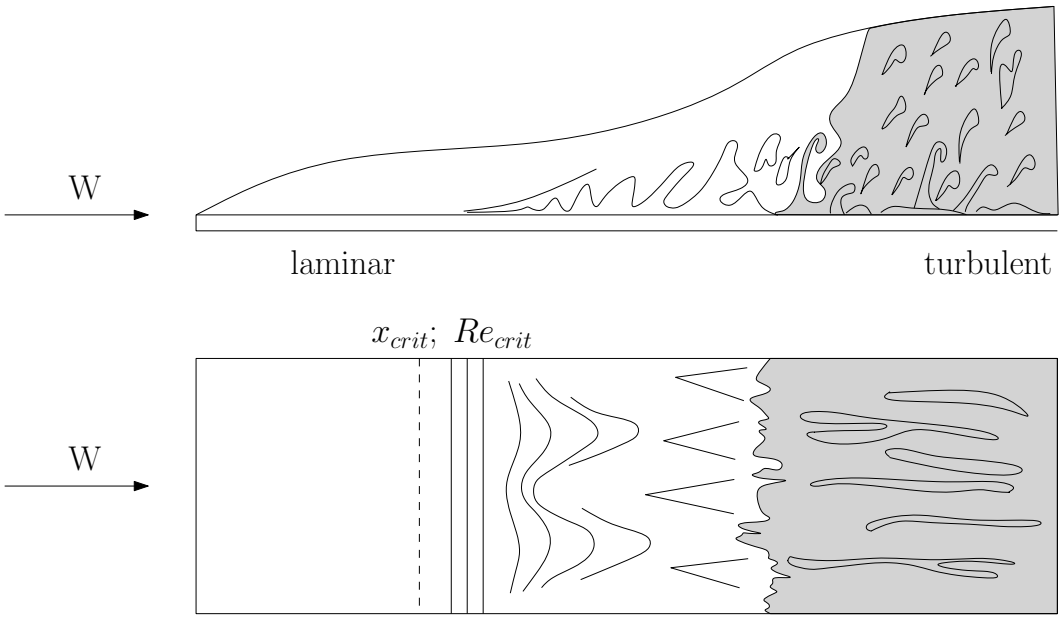

Figure 2.3: Laminar turbulent turnover.(figure from Oertel (2002))

- continuity equation

$$\frac{1}{r}\frac{\partial(r\overline{U})}{\partial r} + \frac{\partial\overline{W}}{\partial z} = 0 \tag{2.26}$$

- momentum boundary equation into the radial direction

$$0 = -\frac{\partial\overline{P}}{\partial r} + \nu\frac{\partial}{\partial r}\left[\frac{1}{r}\frac{\partial r\overline{U}}{\partial r}\right] - \frac{1}{r}\frac{\partial}{\partial r}\left[r\overline{U'U'}\right] \tag{2.27}$$

- momentum boundary equation into the axial direction

$$\frac{1}{r}\frac{\partial(r\overline{W}\,\overline{U})}{\partial r} + \frac{\partial(\overline{W}\,\overline{W})}{\partial z} = -\frac{\partial\overline{P}}{\partial z} + \frac{1}{r}\frac{\partial}{\partial r}\left[r\left\{\nu\frac{\partial\overline{W}}{\partial r} - \overline{U'W'}\right\}\right] \tag{2.28}$$

- thermal boundary layer equation

$$\frac{1}{r}\frac{\partial(r\overline{T}\,\overline{U})}{\partial r}+\frac{\partial(\overline{T}\,\overline{W})}{\partial z}=\frac{1}{r}\frac{\partial}{\partial r}\left[r\left\{a\frac{\partial\overline{T}}{\partial r}-\overline{U'T'}\right\}\right] \tag{2.29}$$

2.4.1 The structure of the turbulent velocity boundary layer

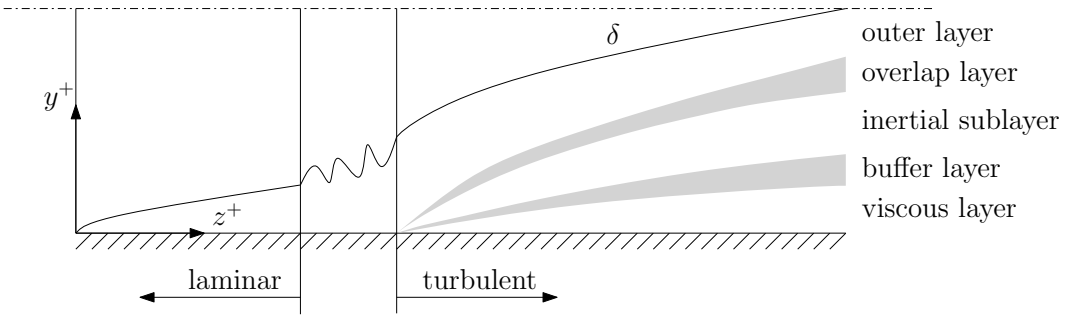

Figure 2.4: The structure of the turbulent velocity boundary layer.

Figure 2.4 shows a typical development of a velocity boundary layer along a solid wall starting from a laminar entry region with a transition to turbulence followed by a fully turbulent flow.

The structure of a turbulent boundary layer can be described based on two length scales, the boundary layer thickness δ, and a characteristic viscous scale $\frac{\nu}{W'}$. The latter was introduced by Tennekes and Lumley (1972), and it relates the kinematic viscosity to a characteristic level of the velocity fluctuation W'.

In a turbulent boundary layer different regions can be distinguished. Figure 2.5 gives an overview of these different layers and the determining length scale ratios.

- Inner layer: This layer, which consists of the viscous sublayer and the buffer layer is located closest to the wall, where the motion is controlled by viscous forces.

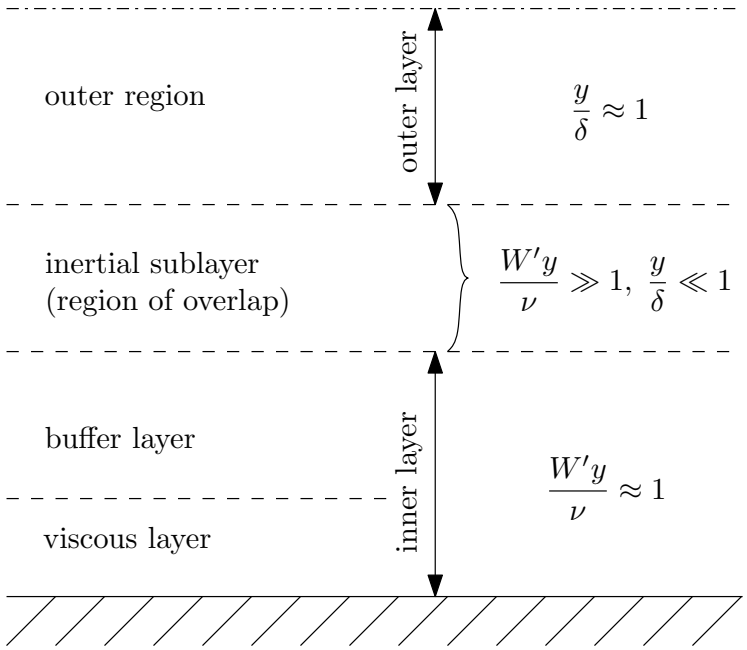

Figure 2.5: Regions of a turbulent boundary layer.

- Inertial sublayer: This represents an intermediate layer which, is neither controlled by viscous forces nor by the outer flow conditions affecting the boundary layer thickness δ.

- Outer layer: This layer is essentially determined by the outer flow conditions, such as the pressure gradient, which depends on the considered flow configuration.

2.4.2 Computation of turbulent boundary layer flow

2.4.2.1 Total shear stress

The non-linear fluctuation term occurring on the righthand side of the turbulent boundary layer equation into the axial direction (eq. (2.28)), can

be considered as a contribution of the turbulent motion to the total shear stress. Accordingly, one can write

$$\frac{1}{r}\frac{\partial(r\overline{WU})}{\partial r} + \frac{\partial(\overline{WW})}{\partial z} = -\frac{\partial \overline{P}}{\partial z} + \frac{1}{\rho r}\frac{\partial}{\partial r}\left[r\left\{\tau_{tot}\right\}\right]$$

with the total shear stress given as

$$\tau_{tot} = \underbrace{\rho\nu\frac{\partial \overline{W}}{\partial r}}_{\tau_{lam}} \underbrace{-\rho\overline{U'W'}}_{\tau_{turb}}. \tag{2.30}$$

Applying the Boussinesq eddy viscosity concept the turbulent shear stress is computed analogously to the viscous counterpart

$$-\overline{U'W'} = \nu_T \frac{\partial \overline{W}}{\partial r} \tag{2.31}$$

introducing an eddy diffusivity of momentum ν_T. The total shear stress can then be rewritten as

$$\tau_{tot} = (\nu + \nu_T)\frac{\partial \overline{W}}{\partial r}. \tag{2.32}$$

The eddy diffusivity of momentum, or eddy viscosity, is a turbulent flow variable and not a material property like the molecular viscosity. As stated in Kays and Crawford (1993), the eddy diffusivity exceeds by far the viscous counterpart in fully turbulent flows, i.e. $\nu_T >> \nu$, except in the viscous sublayer close to the wall, where $\nu >> \nu_T$.
Using Boussinesq's eddy diffusivity approach requires closure for ν_T. A very old well established approach is based on L. Prandtl's (1925) mixing-length

theory. Following Prandtl's concept the turbulent shear stress is obtained as

$$\tau_{turb} = {l_m}^2 \left| \frac{\partial \overline{W}}{\partial y} \right| \frac{\partial \overline{W}}{\partial y} \tag{2.33}$$

with y denoting the distance from the wall

$$y = \frac{D}{2} - r,$$

involving the so called mixing length l_m, which implies that the eddy diffusivity of momentum transfer reads

$$\nu_T = {l_m}^2 \left| \frac{\partial \overline{W}}{\partial y} \right|. \tag{2.34}$$

Oertel (2002) described the mixing length l_m as the length, along which a fluid particle loses its individuality while being mixed up (turbulent) with the surrounding fluid. A very popular mathematical description of l_m was proposed by van Driest (1956) who suggested the following expression

$$l_m = \kappa y \left[1 - e^{\frac{-y}{A}} \right]. \tag{2.35}$$

This expression involves the von Kármán constant κ, and A as empirical parameters.

For the viscous, buffer, and inertial sublayes shown in Figure 2.5 it is possible to find an universal description for the streamwise velocity by normalizing

the flow variables with suitable reference scales. Introducing the wall friction velocity

$$w_\tau = \sqrt{\frac{\tau_w}{\rho}} \tag{2.36}$$

as relevant velocity scale the non-dimensional representation in the so called wall coordinates written as

$$y^+ = \frac{y w_\tau}{\nu}, \tag{2.37}$$

$$W^+ = \frac{W}{w_\tau}, \tag{2.38}$$

$$l_m^+ = \frac{w_\tau l_m}{\nu} = \kappa y^+ \left[1 - e^{\frac{-y^+}{A^+}} \right] \tag{2.39}$$

is obtained. Assuming a constant total shear stress in the region near the wall one can write

$$\tau_{tot} \approx \tau_w, \tag{2.40}$$

so that eq. (2.32) combined with (2.34) can be rewritten as

$$1 = \underbrace{\frac{\partial \overline{W^+}}{\partial y^+}}_{\tau_{lam}} + \underbrace{l_m^{+2} \left| \frac{\partial \overline{W^+}}{\partial y^+} \right| \frac{\partial \overline{W^+}}{\partial y^+}}_{\tau_{turb}} \tag{2.41}$$

The solution of eq. (2.41) provides universal laws for $\overline{W}^+$ in the individual sublayers near the wall valid in a certain range of the wall distance y^+.

- 1. Viscous sublayer: $y^+ < 5$
  Inside this layer closest to the wall the viscous forces are dominant and the turbulent shear stress is negligible, so that

  $$\tau_w = \tau_{lam}.$$

  The integration of equation (2.41) yields a simple linear variation of the mean velocity

  $$\overline{W}^+ = y^+. \tag{2.42}$$

- 2. Buffer layer: $5 < y^+ < 50$
  This layer is located between the viscous and the inertial sublayer. Inside this region both the effects of viscous and inertial forces are relevant, which implies that neither of the stresses can be neglected in the integration of eq. (2.41). The universal expression for the streamwise velocity is obtained here as

  $$\overline{W}^+ = \int_0^{y^+} \frac{2\mathrm{d}y^+}{1 + \sqrt{1 + 4{l_m}^{+2}}} \tag{2.43}$$

  using, e. g. the ansatz of van Driest (2.39) for ${l_m}^+$

- 3. Inertial sublayer: $y^+ > 50$
  In the inertial sublayer the distance from the wall is far enough to neglect the viscous forces, and only the turbulent contribution has to be considered. In this region the mixing length can be assumed as linearily dependent of y^+, i.e.,

$$l_m{}^+ = \kappa y^+, \tag{2.44}$$

  which also represents the asymptotic limit of the van Driest equation (2.39) for large y^+. Substituting eq. (2.44) into eq. (2.41) and neglecting the viscous contribution τ_{lam} yields, the so called "law of the wall" or "log law" written as

$$\overline{W}^+ = \frac{1}{\kappa} ln\left(y^+\right) + \beta. \tag{2.45}$$

  The integration constant β and the von Kármán constant are empirically obtained parameters.

- 4. Outer turbulent layer:
  In the outer turbulent layer remote from the wall the mean velocity profile becomes also dependent of the boundary layer thickness δ, which is strongly related to the pressure gradient into the streamwise direction $\frac{\mathrm{d}p}{\mathrm{d}z}$. With the help of experimental data, Coles (1956) proposed a non-universal formulation for this region. Cole introduced an additional term into the "law of the wall" (equation (2.45), which describes the velocity derivation from the law of the wall using an S-shaped profile. The so obtained formula is known as Coles' law of the wake written as

$$\frac{\overline{W}^+}{w_\tau} = f\left(\frac{y w_\tau}{\nu}\right) + \frac{\Pi}{\kappa}\eta\left(\frac{y}{\delta}\right) \tag{2.46}$$

  The first term in equation (2.46) represents the "law of the wall". The second term, which represents the velocity derivation, depends on the

pressure gradient into the axial direction ($\Pi = f\left(\frac{\mathrm{d}p}{\mathrm{d}z}\right)$) as well as on the distance from the wall.

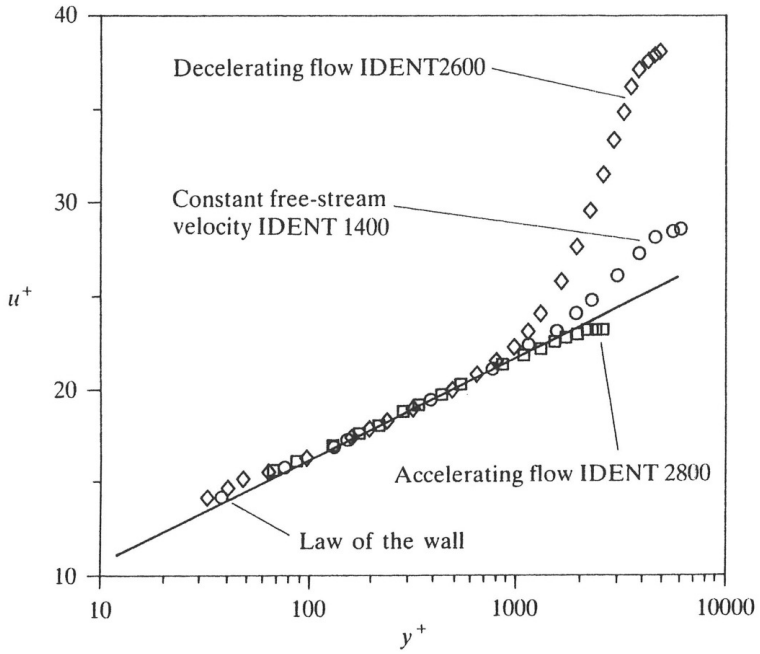

Figure 2.6: The effect of pressure gradient on the turbulent velocity profile (figure from Kays and Crawford (1993))

Figure 2.6 compares flows with different pressure gradients producing decelerating, constant, and accelerating free-stream condition. The deviations from the log-law at large y^+-values are well visible.

2.4.3 Heat transfer in turbulent boundary layer flow

2.4.3.1 Prandtl number

The (molecular) Prandtl number basically represents a non-dimensional material property, which is defined as the ratio of the diffusivity of momentum to the thermal diffusivity.

$$Pr = \frac{c\mu}{\lambda} = \frac{\nu}{a} = \frac{\text{diffusivity of momentum}}{\text{thermal diffusivity}} \tag{2.47}$$

Applying an order-of-magnitude analysis to the non-dimensionalized boundary layer equations for a convective laminar flow along a heated (or cooled) wall it can be shown that the molecular Prandtl number measures the relative thickness of the thermal boundary layer to the velocity boundary layer according to

$$\frac{\delta^2}{\delta_T^2} = O\left(\frac{1}{\sqrt{Pr}}\right). \tag{2.48}$$

The streamwise development of the boundary layer thickness along a flat plate is exemplary shown for different Prandtl numbers in figure 2.7.
The relation (2.48) is, strictly speaking, only valid in laminar flow. It can be, however, extended to the turbulent flow as well, where it applies to the relative thicknesses of the corresponding viscous sublayers.

2.4.3.2 Turbulent Prandtl number

As outlined above the molecular Prandtl number relates by definition the molecular diffusive transport of momentum caused by the viscous forces to the molecular conductive transport of heat. Analogously, a turbulent Prandtl number can be defined as the ratio of the eddy diffusivity of momentum to the eddy conductivity written as

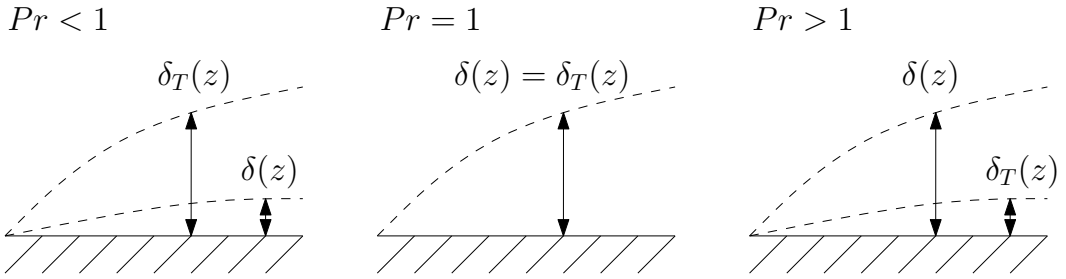

Figure 2.7: Velocity and thermal boundary layers with different molecular Prandtl numbers.

$$Pr_T = \frac{\nu_T}{a_T}. \tag{2.49}$$

As such it relates the turbulent transfer of momentum associated with the turbulent stresses to the turbulent transfer of heat associated with the turbulent convective heat flux terms

$$\overline{U'W'} \leftrightarrow \overline{U'T'}.$$

In contrast to the molecular Prandtl number the turbulent Prandtl number is no material property. Based on experimental studies it is mostly assumed as constant of the order of $Pr_T \sim 0.9$. Nevertheless, it is known that the turbulent Prandtl number can deviate considerably from this value close to the wall. Since it is often used to compute the eddy conductivity a_T in terms of the eddy viscosity ν_T, it represents an important input parameter for the modelling of the turbulent heat transfer. Therefore, the present work puts a special focus on the variation of the turbulent Prandtl number near the wall in the analysis of the numerical results.

2.4.3.3 Reynolds analogy

The Reynolds analogy basically represents a concept, which allows to compute the solution of the thermal boundary layer equation directly from the solution of the velocity boundary layer equation. It is strictly speaking only applicable to boundary layer flow along flat plates, when the following assumptions can be made:

- steady state
- incompressible fluid
- no pressure gradient into the streamwise direction
- viscous heating negligible
- constant wall temperature, $T_w = const$
- unity molecular Prandtl number, $Pr = 1$
- unity turbulent Prandtl number, $Pr_T = 1$

Under these conditions the non-dimensional solution for the velocity and temperature are identical, i. e. ,

$$\overline{W}^* = \frac{\overline{W}}{W_\infty} = \overline{T}^* = \frac{T_w - \overline{T}}{T_w - T_\infty} \,, \tag{2.50}$$

where W_∞ and T_∞ represent the free-stream velocity and temperature, respectively.
Based on the identity (2.50) all derived quantities like wall friction and wall heat flux can be directly related to each other.
In case of a heated pipe flow, the Reynolds analogy is not applicable, because the pressure gradient term occurring in the momentum equation has no analogous counterpart in the energy equation.

2.4.3.4 Total heat flux

In analogy to the shear stress in the momentum equation the leading-order convective fluctuation term in the thermal boundary layer equation

(equation (2.29)) can be interpreted as a turbulent contribution to the total heat flux, such that

$$\frac{1}{r}\frac{\partial(r\overline{T}\,\overline{U})}{\partial r}+\frac{\partial(\overline{T}\,\overline{W})}{\partial z}=\frac{1}{r}\frac{\partial}{\partial r}\left[r\left\{-q_{tot}\right\}\right]$$

with

$$\frac{q_{tot}}{\rho c}=\underbrace{-a\frac{\partial\overline{T}}{\partial y}}_{q_{lam}}+\underbrace{\overline{U'T'}}_{q_{turb}}. \tag{2.51}$$

Applying Boussinesq's eddy diffusivity concept to the turbulent heat flux contribution we obtain

$$\overline{U'T'}=-a_T\frac{\partial\overline{T}}{\partial y}, \tag{2.52}$$

$$q_{tot}=-\left(a+a_T\right)\frac{\partial\overline{T}}{\partial y} \tag{2.53}$$

involving the turbulent eddy conductivity a_T.

Analogously to the wall friction velocity defined by equation (2.36) a wall temperature defined as

$$T_\tau=\frac{q_w}{\rho c w_\tau} \tag{2.54}$$

is introduced as reference scale for rewriting the temperature in non-dimensional wall coordinates as

$$\theta^+ = \frac{T_w - T}{T_\tau}. \tag{2.55}$$

Similar to the total shear stress it is assumed that the total heat flux remains constant in the wall region, so that

$$q_{tot} = const. = q_w. \tag{2.56}$$

Analogously to the velocity boundary layer an universal solution can be computed for the individual sublayers near the wall.

- 1. Viscous sublayer: $y^+ Pr < 5$
  Inside this layer next to the wall the laminar heat flux is dominant, and the turbulent heat flux can be neglected, so that

  $$q_{tot} = q_w = q_{lam}.$$

  Using this assumption in equation (2.53) the temperature is obtained as

  $$\overline{\theta}^+ = Pry^+. \tag{2.57}$$

- 2. Inertial sublayer: $y^+ Pr > 50$
  Inside this sublayer the influence of the viscous heat flux is negligible compared to the turbulent heat flux, so that

  $$q_{tot} = q_w = q_{turb}.$$

Using this assumption in equation (2.53) and rewriting the eddy conductivity in terms of the eddy diffusivity of momentum and the turbulent Prandtl number, i. e. ,

$$a_T = \frac{\nu_T}{Pr_T},$$

the temperature profile can be determined as

$$\overline{\theta}^+ = \frac{Pr_T}{\kappa} ln\left(y^+\right) + \beta_\theta(Pr). \tag{2.58}$$

The integration constant β_θ, which is mainly dependent of the molecular Prandtl number, essentially represents the thermal resistance of the viscous sublayer.

2.5 Heated turbulent pipe flow

2.5.1 Hydraulic entrance region

Unlike in external flow along flat plates, where the boundary layer continuously grows in streamwise direction, in a pipe flow the growth of the boundary layer thickness is limited due to geometrical constraints. The axial distance, which is needed to reach a fully developed flow is called "entrance region". As sketched in Figure 2.8, the entrance region essentially ends, when the boundary layers growing from the wall reach the center.

In the fully developed flow regime downstream of the entrance region the mean velocity profile is independent of the streamwise direction, so that

$$\frac{\partial \overline{U}_i}{\partial z} = 0, \quad \frac{\partial^2 \overline{U}_i}{\partial z^2} = 0.$$

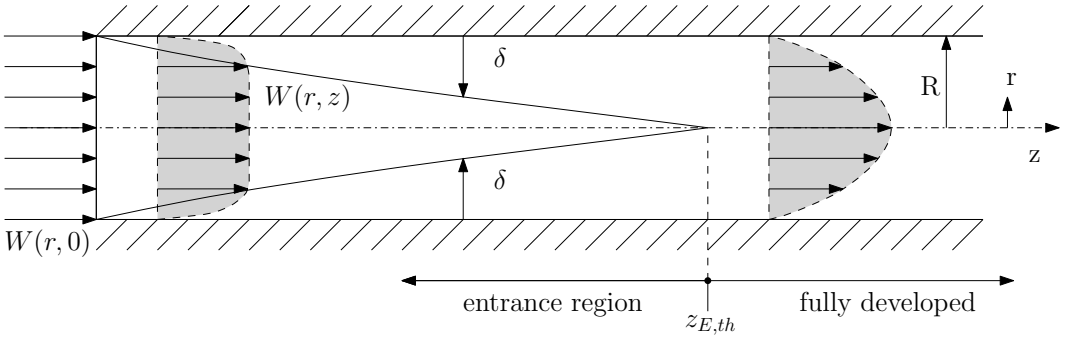

Figure 2.8: Entrance region of a pipe flow.

The integration of the continuity equation gives a zero mean radial velocity component

$$\overline{U} \equiv 0.$$

According to the literature the entrance length in turbulent pipe flow varies around 50 to 60 pipe diameters.

2.5.2 Thermal entrance region

The present study considers the case of a turbulent pipe flow, which is heated with a constant wall heat flux, as sketched in Figure 2.9. Due to the uniform input of heat the temperature is continuously increasing in the streamwise direction. The transformation which yields an axially periodic representation of the temperature, will be explained in the following. The advantage of such a transformation is that the transformed temperature allows for the application of periodic thermal boundary conditions into the axial direction.

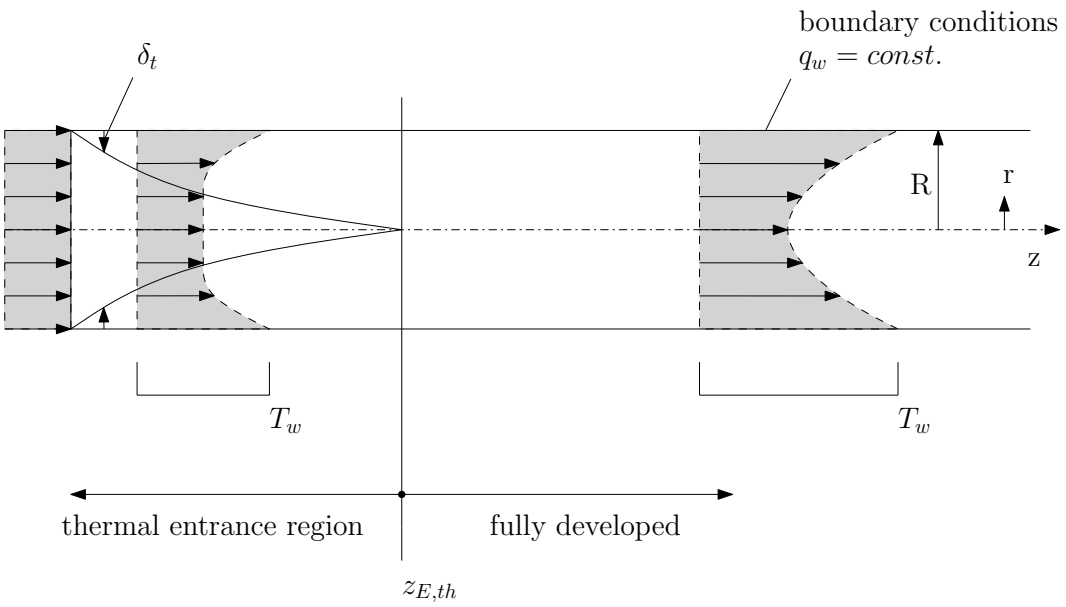

Figure 2.9: Thermal entrance region of a heated pipe flow.(figure from Brenn and Meile (2009))

2.5.2.1 Definition of cross-sectional mean values

At first some reference values shall be defined, which are needed for non-dimensionalization.

In pipe flow there is no free-stream velocity outside the boundary layer, which can be used as reference velocity like in an external flow over a profile. Therefore, the mean velocity, which is equivalent to the volumetric flow rate, is used here as reference scale. It is defined as

$$\overline{w}_m = \frac{\dot{V}}{A} = \frac{1}{A} \int_A \overline{W}(r) \mathrm{d}A. \tag{2.59}$$

Analogously, based on the enthalpy flow across a pipe cross-section, the

mean temperature is defined as

$$\overline{T}_m = \frac{1}{\dot{m}} \int_A \rho \overline{W}(r) \overline{T} \mathrm{d}A = \frac{1}{\overline{w}_m A} \int_A \overline{W}(r) \overline{T} \mathrm{d}A \tag{2.60}$$

involving the mass flow through the pipe written as

$$\dot{m} = \rho \overline{w}_m A. \tag{2.61}$$

2.5.2.2 Conditions for a thermally developed flow with constant heat flux

If appropriate reference quantities are used for non-dimensionalisation, the thermally developed state can be described by a non-dimensional representation of the temperature distribution, which is independent of the axial direction, such that

$$\frac{\partial}{\partial z} \left[\frac{T_w(z) - \overline{T}(r,z)}{T_w(z) - \overline{T}_m(z)} \right] = 0. \tag{2.62}$$

Since the non-dimensional temperature shown in eq. (2.62) is independent of the axial direction, its derivative into the radial direction is also independent of the axial direction. Furthermore, it can be shown that in a thermally developed state the heat transfer coefficient is constant, so that

$$\frac{\alpha}{\lambda} \neq f(z).$$

This implies for the case of constant heat flux (figure 2.10) that the axial change of the temperature at the wall is the same as the change of the mean temperature, since

$$\frac{q_w}{\alpha} = \text{ const. } = (T_w - \overline{T}_m),$$

$$\frac{\mathrm{d}T_w}{\mathrm{d}z} = \frac{\mathrm{d}\overline{T}_m}{\mathrm{d}z}. \tag{2.63}$$

Incorporating eq. (2.63) into eq. (2.62) yields

$$\frac{\mathrm{d}\overline{T}}{\mathrm{d}z} \neq f(z)$$

The axial variation of the mean fluid temperature $\overline{T}_m(z)$ can be easily derived from a global energy balance written as

$$\dot{Q} = \dot{m}c(\overline{T}_{m\,out} - \overline{T}_{m\,in}). \tag{2.64}$$

Rewriting eq. (2.64) for a differential cylindrical element of height dz yields

$$d\dot{Q} = \dot{m}c\left(\frac{\mathrm{d}\overline{T}_m}{\mathrm{d}z}\mathrm{d}z\right) = q_w D\pi \mathrm{d}z,$$

$$\frac{\mathrm{d}\overline{T}_m}{\mathrm{d}z} = \frac{q_w D\pi}{\dot{m}c} \tag{2.65}$$

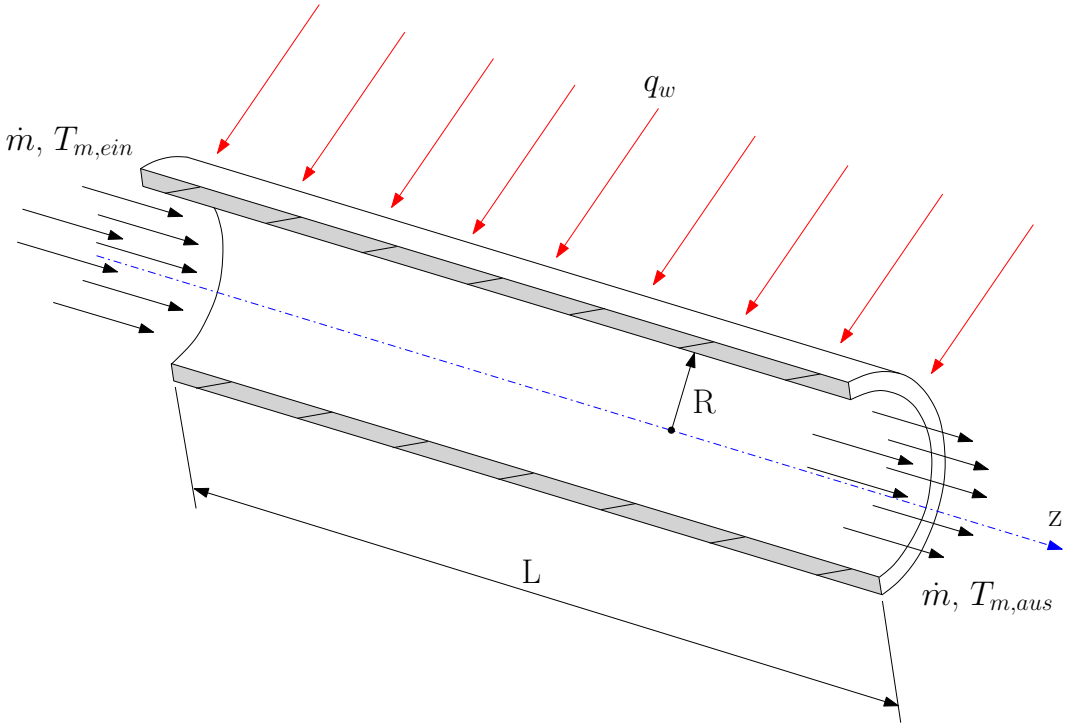

Figure 2.10: Pipe flow with constant heat flux.

with

$$\dot{m} = \frac{\rho D^2 \pi}{4} \overline{w}_m.$$

The integration of eq. (2.65) gives

$$\overline{T}_m(z) = \overline{T}_{m\,in} + \frac{q_w 4}{D \rho c \overline{w}_m} z \tag{2.66}$$

This equation describes the linear axial variation of the mean temperature

along the pipe, where the first part is the mean temperature at the entrance and the second part is the temperature rise due to constant heat flux.

Introducing the following decomposition

$$T(t;r,\phi,z) = T_w(z) - \theta(t;r,\phi,z) \tag{2.67}$$

into the balance equation of energy (2.14) yields

$$\begin{aligned} \frac{\partial\theta}{\partial t} + U\frac{\partial\theta}{\partial r} + \frac{V}{r}\frac{\partial\theta}{\partial\phi} + W\left(-\frac{\mathrm{d}T_w}{\mathrm{d}z} + \frac{\partial\theta}{\partial z}\right) = \\ +a\left[\frac{1}{r}\frac{\partial}{\partial r}\left(r\frac{\partial\theta}{\partial r}\right) + \frac{1}{r^2}\frac{\partial^2\theta}{\partial\phi^2} + \frac{\partial^2\theta}{\partial z^2}\right] \end{aligned} \tag{2.68}$$

Normalizing this equation by introducing the following non-dimensional quantities

$$t^* = \frac{tw_\tau}{D},\ r^* = \frac{r}{D},\ z^* = \frac{z}{D},\ p^+ = \frac{p}{\rho {w_\tau}^2},$$
$$U^+ = \frac{U}{w_\tau},\ V^+ = \frac{V}{w_\tau},\ W^+ = \frac{W}{w_\tau},$$

$$\theta^+ = \frac{\theta}{T_\tau},$$

and recalling equation (2.63) yields

$$\frac{\partial \theta^+}{\partial t^*} + U^+ \frac{\partial \theta^+}{\partial r^*} + \frac{V^+}{r^*} \frac{\partial \theta^+}{\partial \phi} + W^+ \frac{\partial \theta^+}{\partial z^*} = \\ + \frac{1}{Re_\tau Pr} \left[\frac{1}{r^*} \frac{\partial}{\partial r^*} \left(r^* \frac{\partial \theta^+}{\partial r*} \right) + \frac{1}{r^{*2}} \frac{\partial^2 \theta^+}{\partial \phi^2} + \frac{\partial^2 \theta^+}{\partial z^{*2}} \right] + W^+ \underbrace{\frac{\mathrm{d}T_w^+}{\mathrm{d}z^*}}_{=\frac{\mathrm{d}\overline{T}_m{}^+}{\mathrm{d}z^*}=\frac{4}{\overline{w}_m{}^+}}, \tag{2.69}$$

where $Re_\tau = \dfrac{w_\tau D}{\nu}$ is the Reynolds number based on the wall friction velocity.

Using the formulation (2.69) the boundary condition can be written as

- at the wall: $r^* = R^*$

$$\theta^+ = 0 \tag{2.70}$$

- at the center of the pipe: $r^* = 0$

$$\theta^+ = \frac{1}{2} \left(\theta^+(r^*_{in}, \phi, z^*) + \theta^+(r^*_{in}, \phi + \pi, z^*) \right) \tag{2.71}$$

  with r^*_{in} being the radius of the first grid cell next to the center of the pipe.
- periodic in ϕ

$$\theta^+ \left(r^*, \phi, z^* \right) = \theta^+ \left(r^*, \phi + 2\pi, z^* \right) \tag{2.72}$$

- periodic in z^*

$$\theta^+ \left(r^*, \phi, z^* + \frac{L}{D} \right) = \theta^+ \left(r^*, \phi, z^* \right) \tag{2.73}$$

with L being the axial length of the domain.

2.5.3 Total shear stress

Based on the radial variation of the total shear stress in a turbulent pipe flow it is possible to check, if the flow has reached a statistically stationary and fully developed state. In a statistically stationary and fully developed turbulent pipe flow the mean pressure is only dependent of the streamwise position $\overline{P}^+ = \overline{P}^+(z^*)$ and the Reynolds averaged axial momentum equation reads

$$0 = -\frac{\mathrm{d}\overline{P}^+}{\mathrm{d}z^+} + \frac{1}{r^*}\frac{\partial}{\partial r^*}\left(r^* {\tau_{tot}}^+\right) \tag{2.74}$$

The integration of this equation yields

$$\frac{\tau_{tot}}{\rho {w_\tau}^2} = {\tau_{tot}}^+ = \frac{r^*}{2}\frac{\mathrm{d}\overline{P}^+}{\mathrm{d}z^*} \tag{2.75}$$

Applying a simple force balance the mean pressure gradient can be related to the wall shear stress through

$$\frac{\mathrm{d}\overline{P}}{\mathrm{d}z}\frac{D^2\pi}{4} = \tau_w D\pi, \tag{2.76}$$

which can be rewritten in non-dimensional form as

$$\frac{\mathrm{d}\overline{P}^+}{\mathrm{d}z^*} = 4, \tag{2.77}$$

so that

$$\tau_{tot}{}^{+} = \frac{\tau}{\tau_w} = 2r^*. \tag{2.78}$$

In figure 2.11, radial variation of the total shear stress and of its components, the laminar and turbulent shear stress, can be seen. The profiles for both components are obtained from a DNS at $Re_\tau = 360$.
The laminar shear stress reaches its maximum at the wall, while the turbulent shear stress resulting from the turbulent fluctuations (see equation (2.30)), vanishes due to the viscous damping of the turbulent motion.

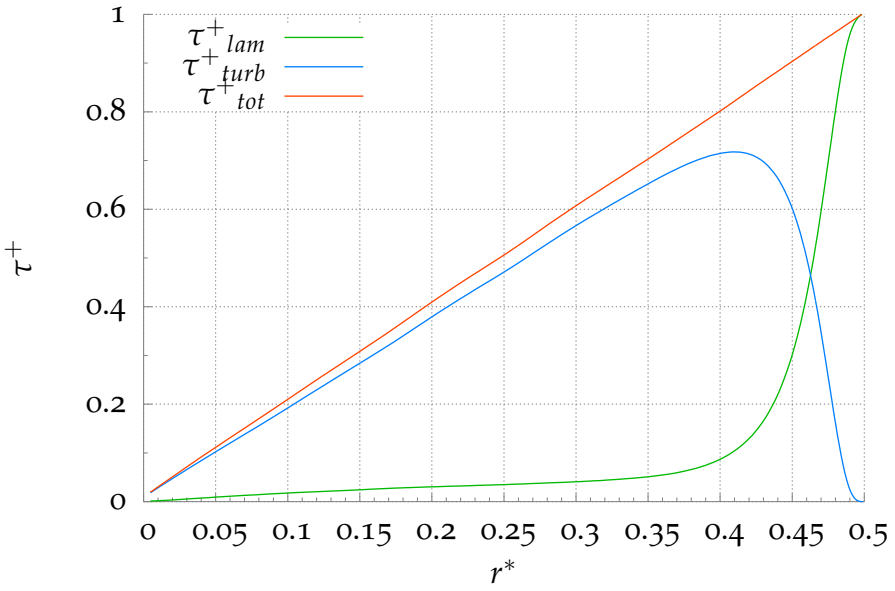

Figure 2.11: Total shear stress with its components, the laminar and turbulent shear stress.

2.5.4 Wall heat transfer

For a hydraulically and thermally fully developed pipe flow the Reynolds averaged representation of the non-dimensional energy equation (2.69)

becomes

$$0 = -\frac{1}{r^*}\frac{\partial}{\partial r^*}(r^* {q_{tot}}^+) - \frac{\overline{W}^+}{{\overline{w}_m}^+}4\,, \tag{2.79}$$

whose integration yields

$$\frac{q_{tot}}{q_w} = {q_{tot}}^+ = -\frac{1}{r^*}\frac{4}{{\overline{w}_m}^+}\int_0^{r^*} r^* \overline{W}^+ \mathrm{d}r^*. \tag{2.80}$$

Figure 2.12 shows the variation of the total heat flux and the viscous and turbulent components along the radial direction. The shown profiles are obtained from a DNS at $Re_\tau = 360$ and $Pr = 1$.

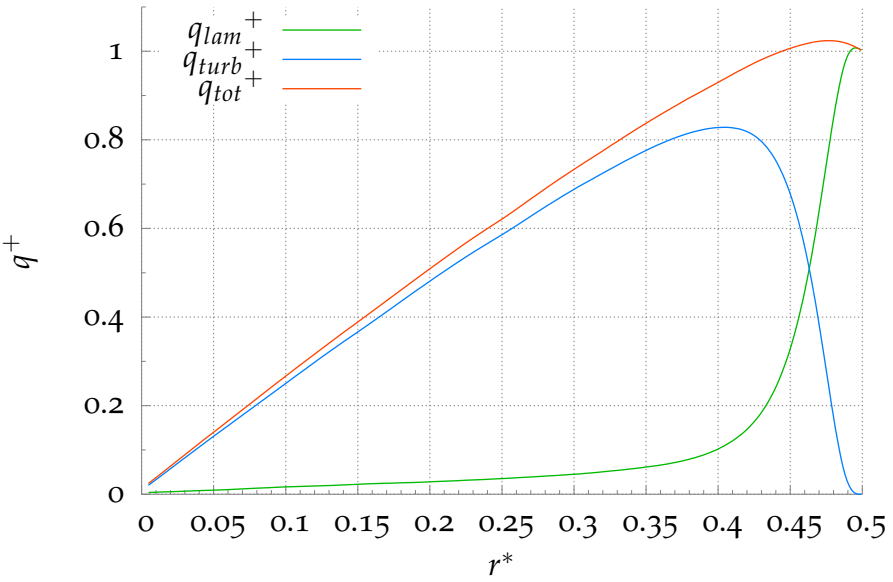

Figure 2.12: Total heat flux with its components, the laminar and turbulent heat fluxes, vs. radius.

2.5.5 Nusselt number

The Nusselt number basically represents a non-dimensional convective heat transfer coefficient. It is defined as the ratio of the convective to conductive heat-transfer.

$$Nu_D = \frac{\alpha D}{\lambda} = \frac{\text{Convective heat transfer}}{\text{Conductive heat transfer}} \tag{2.81}$$

Using the wall heat flux written as

$$q_w = \alpha(T_w - \overline{T}_m) = -\lambda \frac{\partial \overline{T}}{\partial y}\bigg|_{y=0}$$

the Nusselt number can be obtained from the temperature as

$$Nu_D = \frac{\alpha D}{\lambda} = \frac{-\lambda \left.\dfrac{\partial \overline{T}}{\partial y}\right|_{y=0}}{\dfrac{\lambda}{D}\left(T_w - \overline{T}_m\right)}.$$

In most typical engineering flow applications the numerical or analytical computation of the Nusselt number is impossible or too complex. It is therefore common to use empirical correlations to obtain Nu. In case of a pipe flow the Dittus-Boelter equation is a very popular approach:

$$\begin{aligned} 0.7 \;&\leq\; Pr \;\leq\; 160 \\ Re_D = \frac{\overline{w}_m D}{\nu} \;&>\; 10000 \\ \frac{L}{D} \;&\geq\; 10 \end{aligned}$$

$$Nu = \frac{\alpha D}{\lambda} = 0.023 {Re_D}^{4/5} Pr^n \tag{2.82}$$

- $n = 0.4$ if $T_w > \overline{T}_m$
- $n = 0.3$ if $T_w < \overline{T}_m$

3 Numerical model

In this chapter the computational model, which was used in this thesis will be described in detail. The task was to simulate directly a turbulent heated pipe flow to provide valuable data for an evaluation of the existing wall models. The DNS represents the most accurate approach for the simulation of turbulent flow. As such the method gives a most detailed and comprehensive insight into the instantaneous velocity and temperature fields. The simulations were carried out using a simulation code written in Fortran parallelized with MPI. The code solves the transport equations using a finite-volume-method with second-order accuracy in space and time.

3.1 Computational mesh

The configuration investigated in this thesis, is a cylindrical pipe with a length of 5 diameters, which is assumed to be sufficient to capture the largest turbulent structures in the streamwise direction.
An important prerequisite to perform a reliable direct numerical simulation is the generation of a sufficiently fine mesh to resolve all relevant processes and phenomena. Owing to the fact that the relevant flow structures become smaller near the wall the spatial resolution has to be increased towards the wall. For this reason, the grid is clustered in the radial direction towards the wall, while an equidistant grid is used in the axial and azimuthal directions, respectively. In figure 3.1 the computational grid is schematically shown, where the coordinate r stands for the radial, ϕ for the azimuthal, and z for the axial direction, associated with the indices i,j, and k, respectively. The corresponding velocities are U, V, and W.

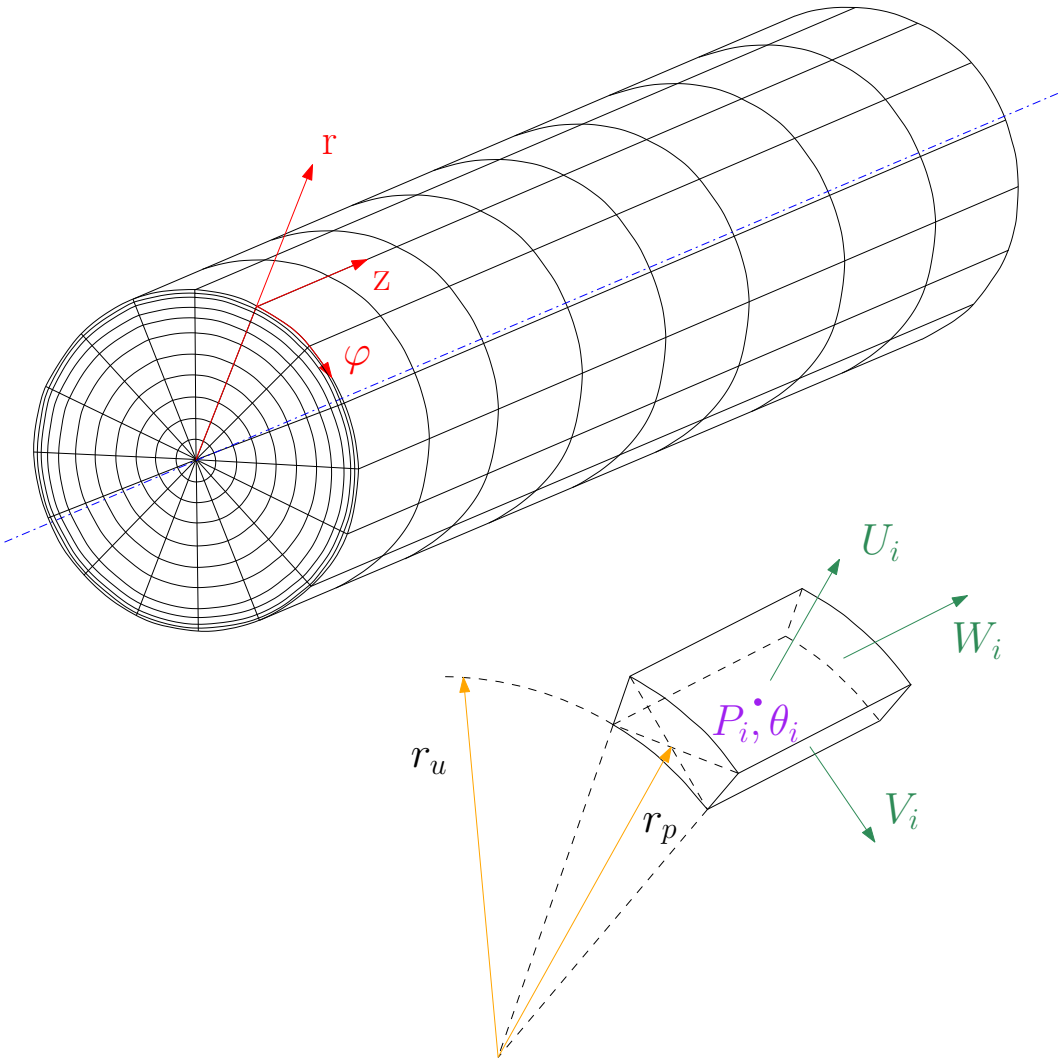

Figure 3.1: Computational grid.

As for the local position of the individual flow quantities a staggered grid is used. This means that the scalar values (pressure and temperature) are located at the center of the cells, while the velocity components are located on the cell faces.

3.2 Numerical solution of the momentum equations

3.2.1 Discretisation

The Navier-Stokes equations (equation (2.4) - (2.7)) are discretized in space using a second-order accurate finite-volume scheme. For the time integration, all advection and diffusion terms are discretized with an explicit scheme, except for the azimuthal direction, where an implicit Crank-Nicolson scheme is used. Solving implicitly the advective and diffusive transports into the azimuthal direction excludes them from the CFL-based timestep criterion, which would otherwise lead to very small maximum timesteps due to the small azimuthal extension of the grid cells near the center.

3.2.2 Integration in time

Assuming a constant density allows for a solution of the Navier-Stokes equations in the limit of low Mach numbers, where the pressure is computed from a Poisson equation derived from the continuity constraint.
First, we recall the mass and momentum balance equation written in vector form for $\rho = const.$ as

$$\underline{\nabla} \cdot \underline{u} = 0 \tag{3.1}$$

$$\frac{\partial \underline{u}}{\partial t} + \underbrace{\underline{\nabla} \cdot (\underline{u}\,\underline{u})}_{\underline{A} \text{ ... advection}} = -\frac{1}{\rho}\underline{\nabla} P + \underbrace{\nu \underline{\nabla}^2 \underline{u}}_{\underline{D} \text{ ... diffusion}} \quad . \tag{3.2}$$

The code uses a so-called Projection method for solving the Navier-Stokes equations, which works in two steps. In the first step the velocity components are predicted (u^*) using a second-order accurate Leapfrog-scheme

for the discrete integration of the advective and diffusive terms in time neglecting the pressure gradient ($\widetilde{L}$ stands for the actually used discretisation scheme).

$$(1): \frac{\underline{u}^* - \underline{u}^{n-1}}{2\Delta t} = \widetilde{L}\{-\underline{A} + \underline{D}\} \tag{3.3}$$

The second step is the so called pressure correction step, which incorporates the pressure gradient to give the solution on the new time level $\underline{u}^{n+1}$.

$$(2): \frac{\underline{u}^{n+1} - \underline{u}^*}{2\Delta t} = -\frac{1}{\rho}\underline{\nabla} P \tag{3.4}$$

The solution of (3.4) for $\underline{u}^{n+1}$ requires the knowledge of the pressure field. This is obtained by taking the divergence of equation (3.4) and enforcing the continuity constraint for the new velocity field

$$\underline{\nabla} \cdot \underline{u}^{n+1} = 0, \tag{3.5}$$

which yields the Poisson equation for the pressure.

$$\underline{\nabla}^2 P = \frac{\rho}{2\Delta t}\underline{\nabla} \cdot \underline{u}^* \tag{3.6}$$

The Poisson equation (3.6) can be solved by using a poisson-solver. The presently used slover applies a fast Fourier transformation in the axial and azimuthal direction producing a sequence of tridiagonal systems, which can be efficiently solved.

Substituting the pressure obtained from the solution of the Poisson equation into eq. (3.4) finally yields the velocity at the new time step

$$\underline{u}^{n+1} = \underline{u}^{*} - \frac{2\Delta t}{\rho}\underline{\nabla} P. \tag{3.7}$$

As mentioned above, the time-integration is carried out with a Leapfrog-scheme. Applied to a general transient differential equation

$$\frac{\partial f}{\partial t} = g(f, \underline{x}, t)$$

the Leapfrog scheme is written as

$$f^{n+1} = f^{n-1} + 2\Delta t g(f^{n}, \overline{x}, t). \tag{3.8}$$

A more detailed description can be found in Hirsch (1988). The combination of a leapfrog-scheme and a central difference scheme, can result in two decoupled solutions, which satisfy the conservation equations, one at the odd, and the other at even time steps. Performing the integration of the solution at the even time steps, the flux terms on the right-hand side always match the solution at the odd time step and vice versa, may continuously enhance the decoupling of the solutions resulting finally in unstably growing oscillations. To avoid this decoupling an Asselin-filter is applied, which basically exchanges information between adjacent time levels in a diffusion-type transfer. Using this filtering eq. (3.8) is rewritten as

$$f^{n+1} = \overline{f^{n-1}} + 2\Delta t g(f^{n}, \overline{x}, t), \tag{3.9}$$

where the filtered representation of the solution at time level $(n-1)$ is obtained as

$$\overline{f^{n-1}} = f^{n-1} + \gamma \left(\overline{f^{n-2}} - 2f^{n-1} + f^{n} \right) \tag{3.10}$$

involving a diffusion parameter γ presently set to $\gamma = 0.075$.

The drawback of this concept is the damping effect of the filter, which can affect the second-order accuracy.

3.3 Numerical solution of the energy equation

The energy equation given by eq. (2.69) is numerically solved using the same temporal and spatial discretization schemes (second-order accurate Leapfrog and finite-volume scheme) as for the momentum equations.
It is solved right after the momentum equations using the updated axial velocity field for the computation of the source term

$$\frac{4\overline{W}^{+}}{\overline{w_m}^{+}}$$

occurring on its right-hand side.

4 Numerical results

4.1 Considered cases

The following table shows all computationally investigated cases of the present work.

Pr	Re_τ (Re_D)	Number of grid cells $(i \times j \times k)$
1	360 (5328)	$128 \times 160 \times 400$
1	480 (7320)	$128 \times 160 \times 400$
1	700 (10759)	$128 \times 160 \times 400$
2	360 (5328)	$128 \times 160 \times 400$
5.9	360 (5328)	$256 \times 160 \times 400$
10	360 (5328)	$512 \times 160 \times 400$

Table 4.1: Computationally investigated cases.

The first three cases assume always unity Prandtl number, while the Reynolds number is varied from $Re_\tau = 360$ to $Re_\tau = 700$. These simulations were mainly carried out to investigate the effect of the Reynolds number on the flow field near the wall and the wall friction. The latter three cases assume the smallest here considered Reynolds number $Re_\tau = 360$, while the Prandtl number is increased up to $Pr = 10$. These cases are particularly intended to show the influence of the reduced thickness of the viscous thermal sublayer relative to thickness of the viscous sublayer for the velocity as the Prandtl number is increased.

In order to keep the computational costs on an acceptable level different grids were used for the different Prandtl numbers. The number of grid cells, which were used for the different cases can also be seen in the table above.

4.2 Flow field

In this section the flow field is examined with the focus on the conditions near the wall. The shown DNS results were obtained for the first three cases listed in table 4.1 considering the Reynolds numbers $Re_\tau = 360/480/700$.

4.2.1 Near wall conditions

4.2.1.1 Statistical mean values

The presented statistical mean values were all obtained by averaging the instantaneous flow quantities in the two homogeneous directions (ϕ and z, see Figure 3.1), and in time.

Figure 4.1 shows the streamwise velocity component in wall coordinates for the different Reynolds numbers. The laminar velocity profile of the viscous sublayer

$$\overline{W}^+ = y^+$$

and the log-law

$$\overline{W}^+ = \frac{1}{\kappa} ln\left(y^+\right) + \beta$$

with $\kappa = 0.40$ and $\beta = 5.5$ as suggested by Kays and Crawford (1993) are plotted as dotted and dashed lines, respectively, as well. In the viscous sublayer, the *DNS* perfectly reproduces the linear dependence of y^+. At a larger distance to the wall, inside the inertial sublayer, differences are noticeable. The deviations from the log-law decrease with increasing Reynolds number. This tendency is also experimentally observed as will be shown in the next subsection. It also indicates that the inertial sublayer, where the log-law is basically derived, is extended as the Reynolds number is increased (Tennekes and Lumley (1972)).

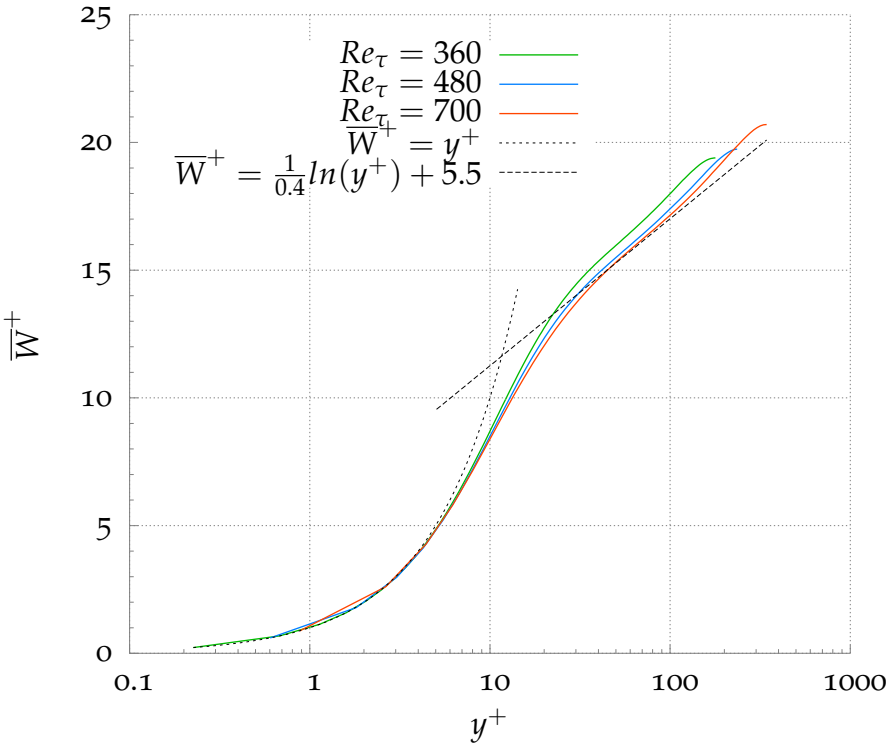

Figure 4.1: Axial velocity for different Reynolds numbers.

Using the *DNS* data it is possible to extract the von Kármán constant based on equation (2.45). For this propose, equation (2.45) had to be differentiated with respect to y^+, which yields the expression

$$\kappa = \frac{1}{y^+} \left(\frac{\partial \overline{W}^+}{\partial y^+} \right)^{-1} . \tag{4.1}$$

The equation (4.1) is evaluated using the local velocity gradients obtained from the *DNS* data, and the resulting κ-profiles are plotted over the wall coordinate y^+ for the different Reynolds numbers in Figure 4.2

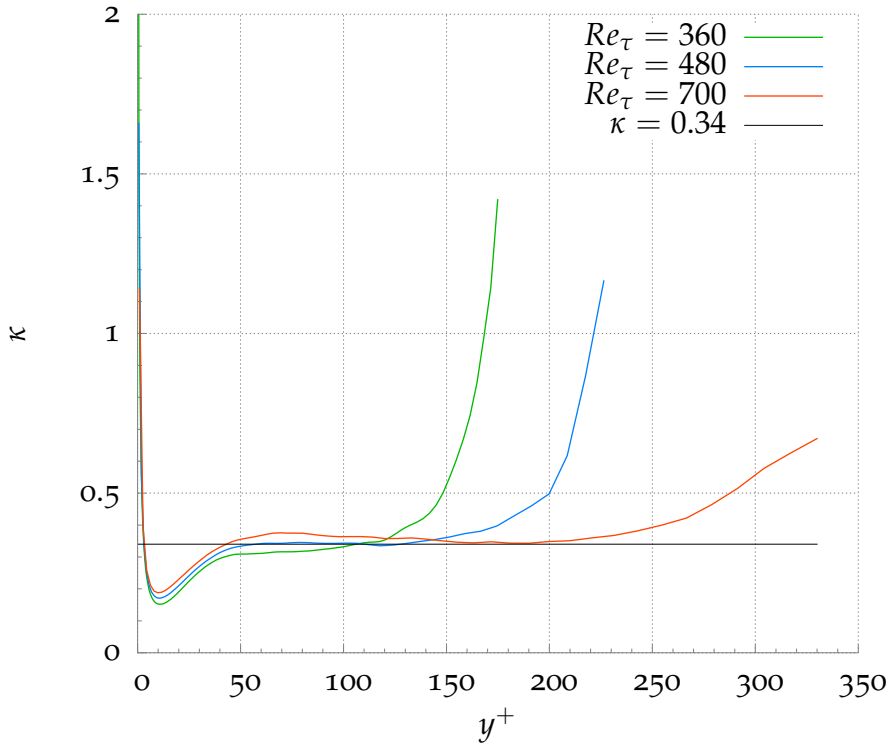

Figure 4.2: Variation of κ in the radial direction obtained from *DNS* results.

One can clearly identify a plateau at $\kappa = 0.34$. This value differs from the κ suggested by Kays and Crawford (1993), which can be explained by the circumstance that the simulations were performed at low Reynolds numbers.

4.2.1.2 Comparison against measurements

Due to the difficulty to measure experimentally all flow quantities very close to the wall, there are hardly any reliable experimental data available for the radial distribution of flow quantities near the wall. Among the scarce studies in literature Durst et al. (1995) published pipe flow measurements, performed at a low Reynolds number ($Re_D = 7442$ / $Re_\tau = 480$) with an outstanding resolution near the wall.
Figures 4.3 compares the mean velocity, as well as the velocity fluctuations obtained in the DNS simulation against the measurements provided by Durst et al. (1995). Only minor deviations are observed, which underlines the the accuracy of the simulation.

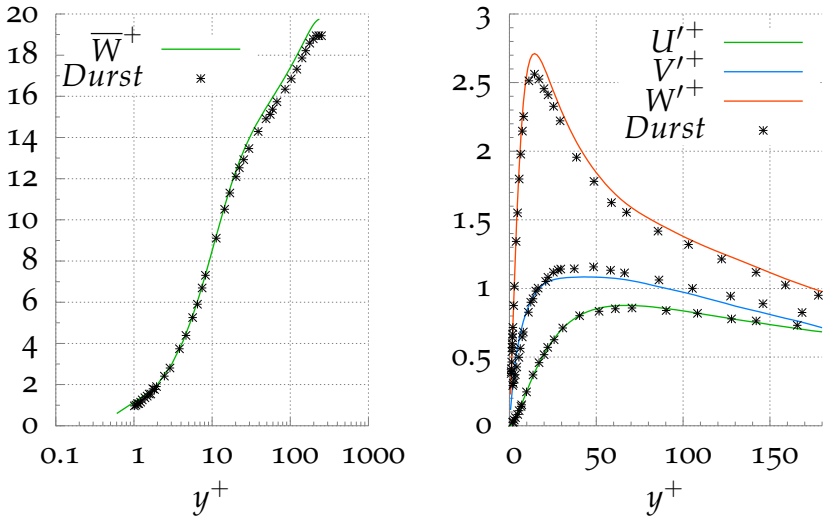

Figure 4.3: Comparison of the axial mean velocity and the velocity fluctuations against measurements of Durst et al. (1995).

Regarding the scope of the log-law in describing the near wall conditions, Durst et al. (1998) published a comparison between measurements from different sources against the log-law for different Reynolds numbers, see figure 4.4. The comparison indicates again that the existence of an inertial sublayer is associated with a sufficiently high Reynolds number. Accordingly, the agreement with the log-law becomes better the higher the Reynolds number.

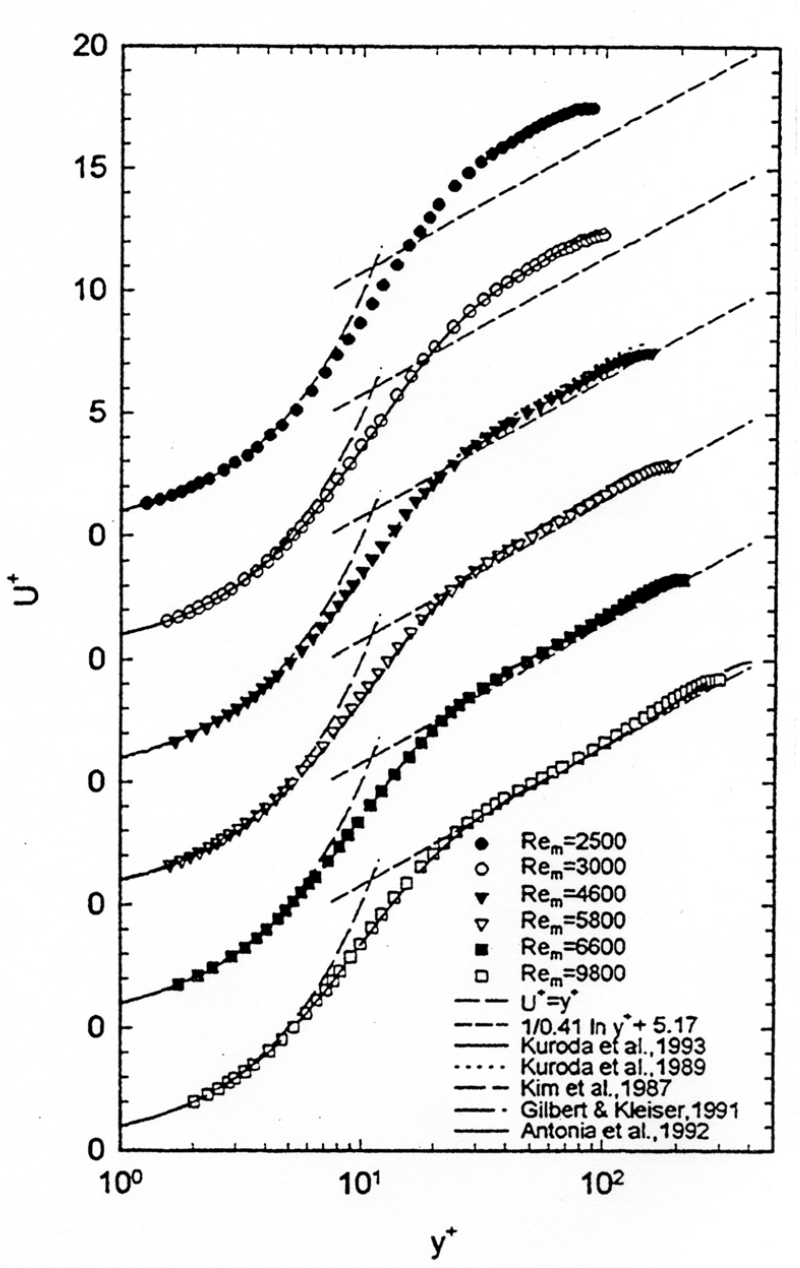

Figure 4.4: Turbulent velocity near the wall, from Durst et al. (1998).

4.2.2 Wall friction

In this section the friction coefficient obtained from the DNS is compared against the most common friction coefficient models. The friction coefficient for the given configuration is computed from the wall shear stress (τ_w) and the bulk mean velocity ($\overline{w}_m$), according to

$$c_f = \frac{\tau_w}{\rho \frac{\overline{w}_m^2}{2}}. \tag{4.2}$$

4.2.2.1 Petukhov

Due to the low values of the Reynolds numbers, considered in this thesis, a friction coefficient model proposed for the transition region between laminar and turbulent motion should be preferably applied. Petukhov et al. (1973) developed a correlation for the friction coefficient, which is valid for

$$\begin{aligned} 2300 \; &< \; Re_D \; < \; 5 \cdot 10^6 \\ 0.5 \; &< \; Pr \; < \; 2000, \end{aligned}$$

and reads

$$c_f = \left(1.58 ln(Re_D) - 3.28\right)^{-2}. \tag{4.3}$$

4.2.2.2 Blasius

For a fully turbulent pipe flow well apart from the laminar-turbulent transition, Blasius proposed a simple model for the friction coefficient, which reads

$$c_f = \frac{0.079}{Re_D^{0.25}}. \tag{4.4}$$

Figure 4.5 compares the friction coefficient predicted by the DNS against the results of the above mentioned correlations.

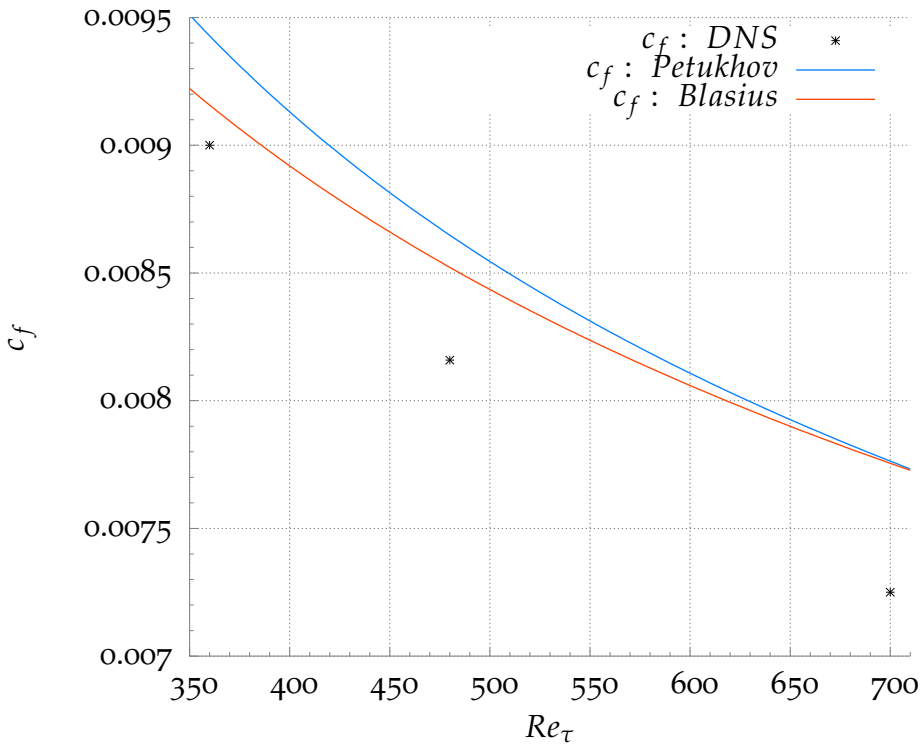

Figure 4.5: c_f obtained from the DNS compared against empirical correlations.

4.3 Temperature field and heat transfer

The variation of the temperature near the wall strongly depends on the Prandtl number. The last three simulation cases listed in table 4.1 were carried out to study the effect of an increase of the Prandtl number up to $Pr = 10$. The Reynolds number was thereby kept always the same $Re_\tau = 360$.

4.3.1 Near wall conditions

4.3.1.1 Statistical mean values

Figure 4.6 shows the mean temperature profiles plotted against the wall coordinate. It becomes evident that the wall gradient of the temperature profile gets steeper with increasing Prandtl number.

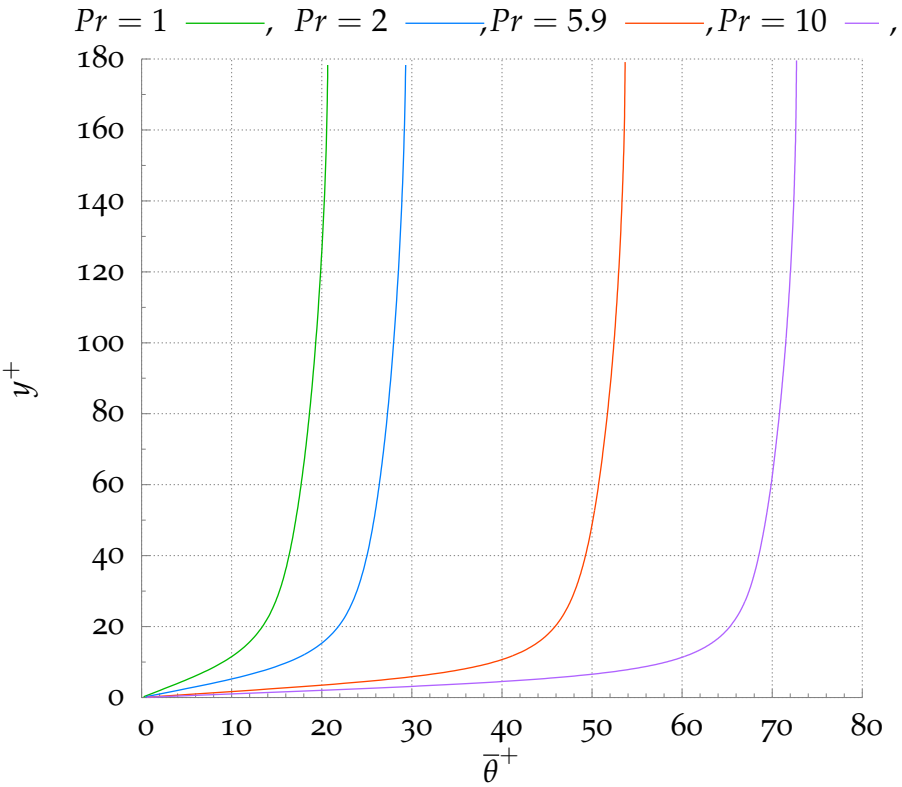

Figure 4.6: Temperature profile for different Prandtl numbers.

Figure 4.7 shows the individual temperature profiles plotted over the wall coordinate in logarithmic scale. The straight parts of the lines indicate the log-law region. Their level is strongly increased as the Prandtl number gets higher.

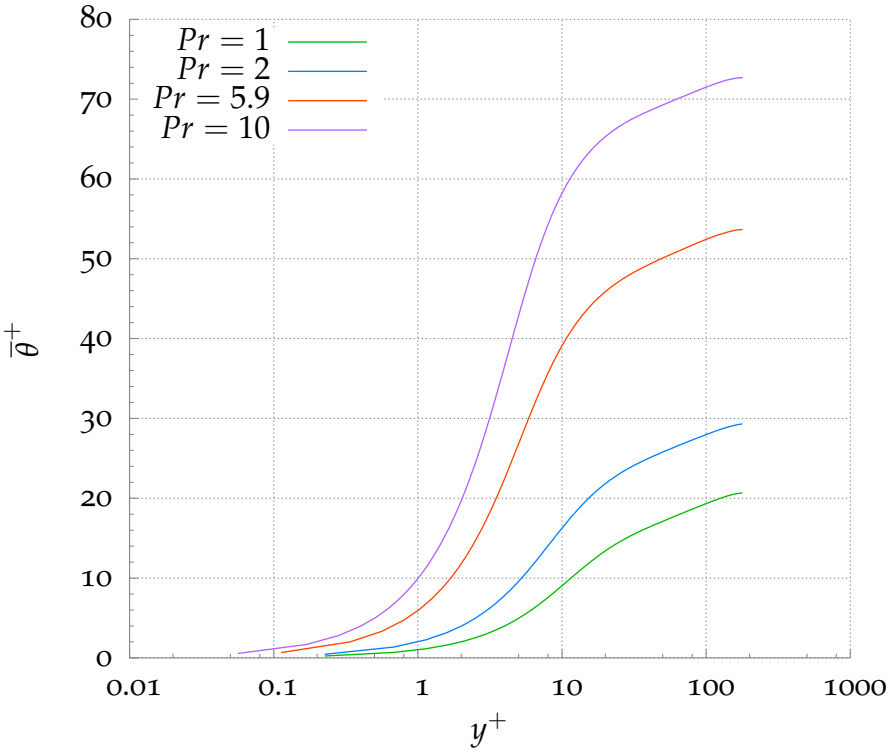

Figure 4.7: Profiles of the temperature $\overline{\theta}^+$ vs. y^+ in semilogarithmic scale for different Prandtl numbers.

4.3.1.2 Turbulent fluctuations

Figure 4.8 shows the mean fluctuation of the non-dimensional temperature obtained as rms-values near the wall for $Pr = 1$. The turbulent intensities of the three velocity components are plotted as well. The near wall variation of the rms-value for the temperature ${\theta'}^+$ is evidently very close to the profile of the turbulent intensity of the streamwise component ${W'}^+$. This is not surprising, as for $Pr = 1$, the non-dimensionalized transport equation for W^+ and θ^+, differ only in the source term on the right-hand side, being

$$\frac{\mathrm{d}P^+}{\mathrm{d}z^*} = 4,$$

and

$$\frac{\mathrm{d}T_w{}^+}{\mathrm{d}z^*} = \frac{\mathrm{d}\overline{T}_m{}^+}{\mathrm{d}z^*} = \frac{4}{\overline{w}_m{}^+},$$

respectively, which is associated with the streamwise periodicity of the solution.

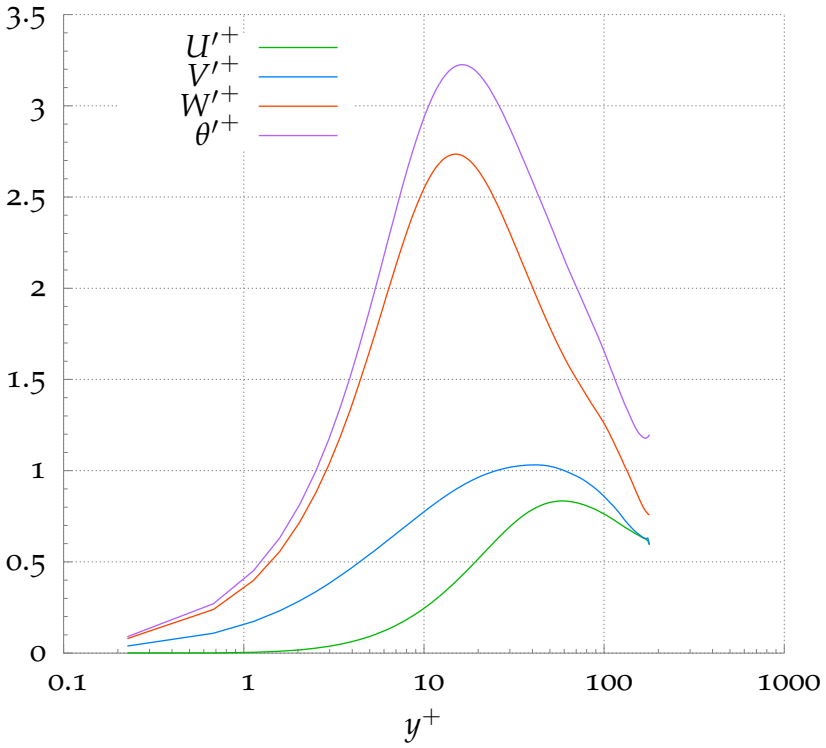

Figure 4.8: Turbulent intensities of temperature and velocity near the wall for Pr=1.

Figure 4.9 shows the mean temperature fluctuations near the wall obtained for the different Pr numbers. The viscous sublayer moves evidently closer to the wall for increasing Pr, and the intensity of the fluctuation gets significantly higher, as seen from the maxima of θ'^+. This behaviour is well in line with the simulation results obtained by Kawamura et al. (1999).

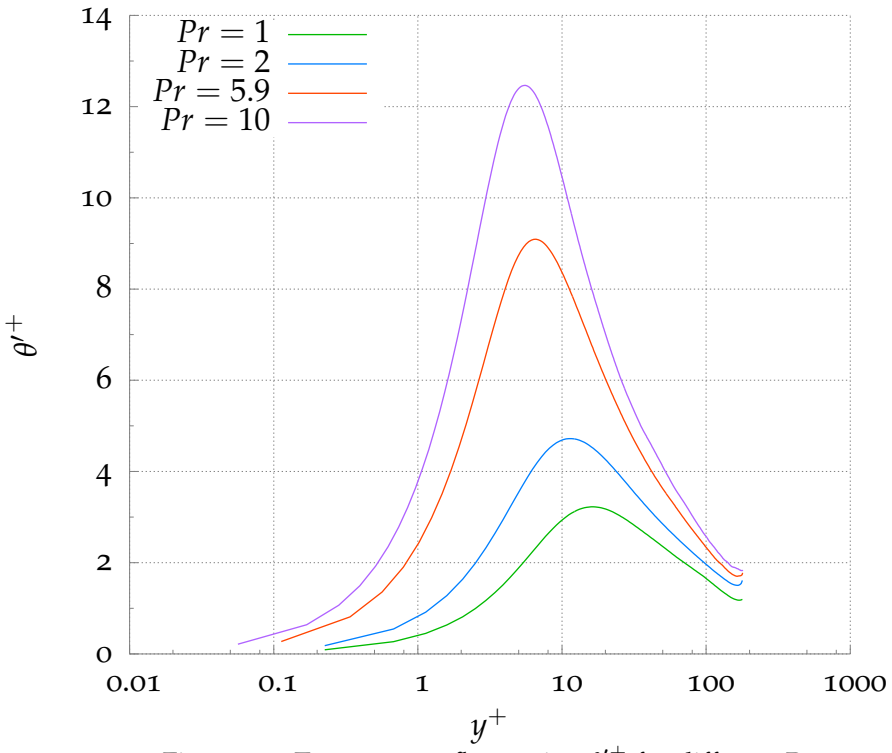

Figure 4.9: Temperature fluctuation θ'^+ for different Pr.

Heat flux

As already stated in chapter 2.4.3.4, the total heat flux is the sum of the laminar and the turbulent heat fluxes (see equation (2.51)). As seen from eq. (2.80), the radial variation of $q_{tot}{}^{+}$ is independent of the Prandtl number. The contributions of the laminar and the turbulent components dependent of the Prandtl number are shown in Figure 4.10. It becomes evident that the contribution of turbulent heat flux becomes relatively higher as the Prandtl number is increased. As already indicated by the temperature fluctuations in Figure 4.9 the sublayer associated with very intense turbulent heat transfer moves closer to the wall the higher the Prandtl number.

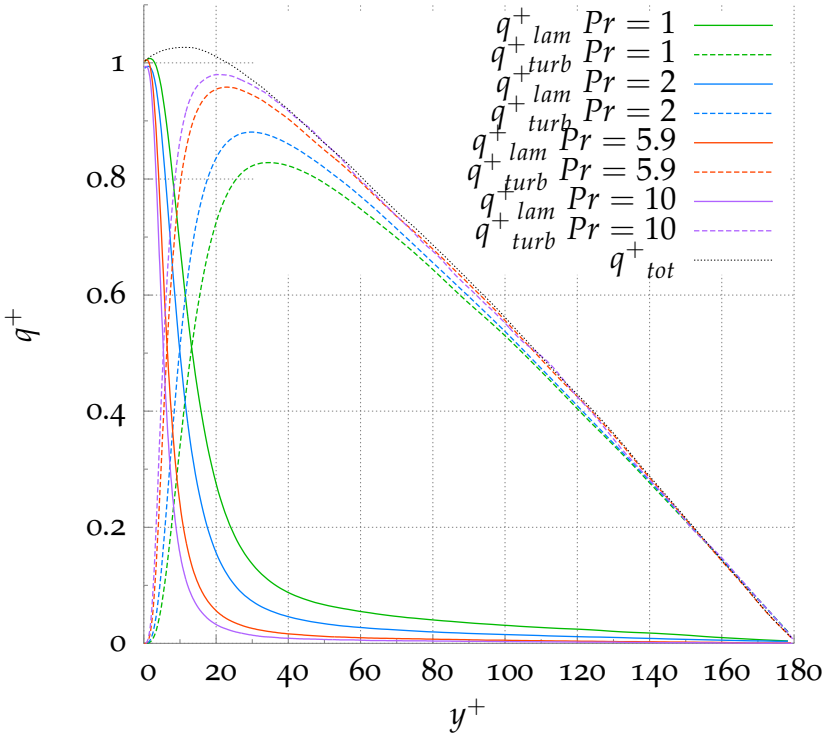

Figure 4.10: Laminar and turbulent heat fluxes vs. y^+ for different Pr.

4.3.1.3 Turbulent Prandtl number

The knowledge of the level of the turbulent Prandtl number and its variation along the radial direction is of paramount importance to obtain accurate models for the heat flux. Based on the DNS data it was possible to calculate the radial variation of the turbulent Prandtl number substituting the local averages of the turbulent flux terms and gradients into the following expression

$$Pr_T = \frac{\nu_T}{a_T} = \frac{\overline{W'^+U'^+}\,\dfrac{\partial\overline{\theta}^+}{\partial y^+}}{\overline{\theta'^+U'^+}\,\dfrac{\partial\overline{W}^+}{\partial y^+}}. \tag{4.5}$$

Figure 4.11 shows the variation of the turbulent Prandtl numbers for different molecular Prandtl numbers computed from eq. (4.5) using the DNS results. The turbulent Prandtl number is fairly low near the center associated with $y^+ > 100$ for all cases. In the inertial regime extending approximately within $10 < y^+ < 100$ the Pr_T profiles are close to unity. For $Pr = 1$ and 2, Pr_T remains approximately constant close to unity also in the viscous sublayer, while the profiles for $Pr = 5.9$ and 10 exhibit a significant increase towards the wall. This indicates that the eddy conductivity a_T decreases faster towards the wall than the eddy diffusivity ν_T as can be seen from the double-logarithmic plot in figure 4.13 and 4.12.

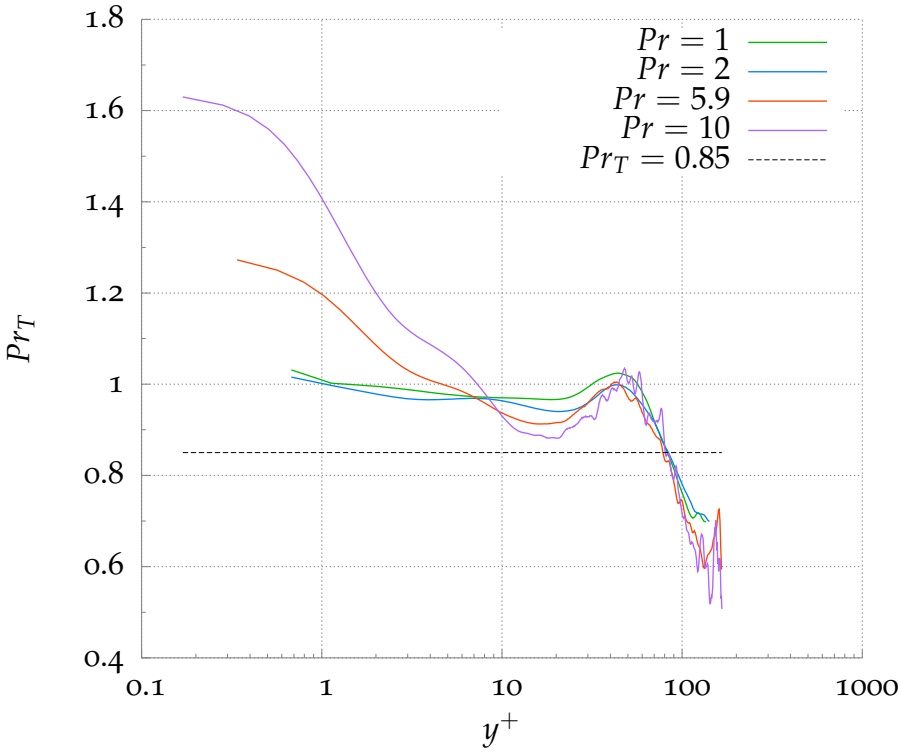

Figure 4.11: Turbulent Prandtl numbers for different Pr.

The reason for the observed faster decrease of the eddy conductivity a_T towards the wall for increasing Prandtl numbers is illustrated in Figure 4.14. The gradients of the non-dimensional temperature shown in the left subfigure approach the constant values

$$\frac{\partial \bar{\theta}^+}{\partial y^+} = Pr$$

as expected in the viscous sublayer near the wall. Consequently, the eddy conductivity near the wall reflects directly the decrease of the turbulent transport $\overline{U'^+\theta'^+}$. As shown in the right subfigure, $\overline{U'^+\theta'^+}$ exhibits a steeper decrease towards the wall for the higher Prandtl numbers, which translates

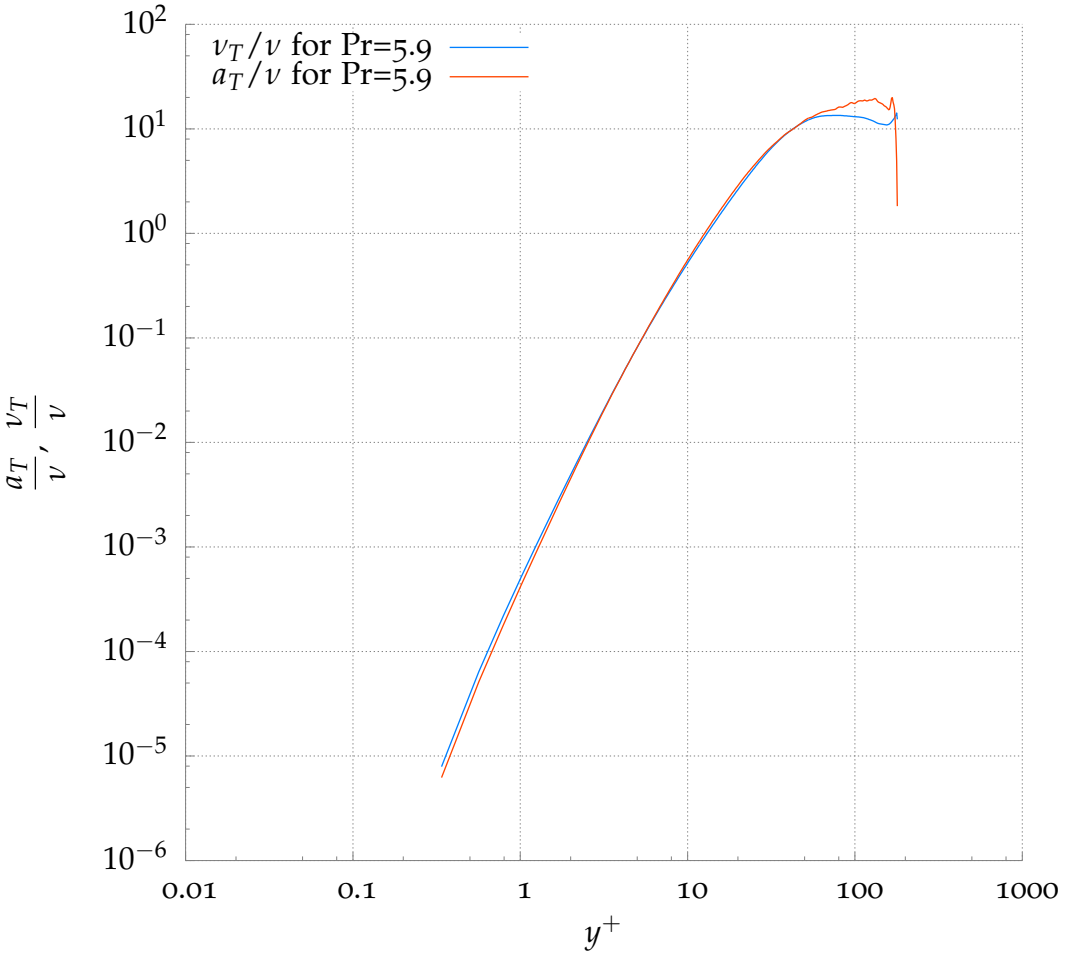

Figure 4.12: Near wall variation of the eddy viscosity and conductivity for $Pr = 5.9$.

directly into a steeper decrease of a_T.

From the results shown in Figure 4.11 it can be finally concluded that the assumption of a constant turbulent Prandtl number, which is commonly made in the models for the turbulent heat flux used in CFD, where it is mostly set to $Pr_T = 0.9$, is essentially confirmed by, the results for the lower molecular Prandtl numbers $Pr = 1$ and 2. For $Pr = 5.9$ and 10 this is clearly not the case in the transition region to the viscous sublayer.

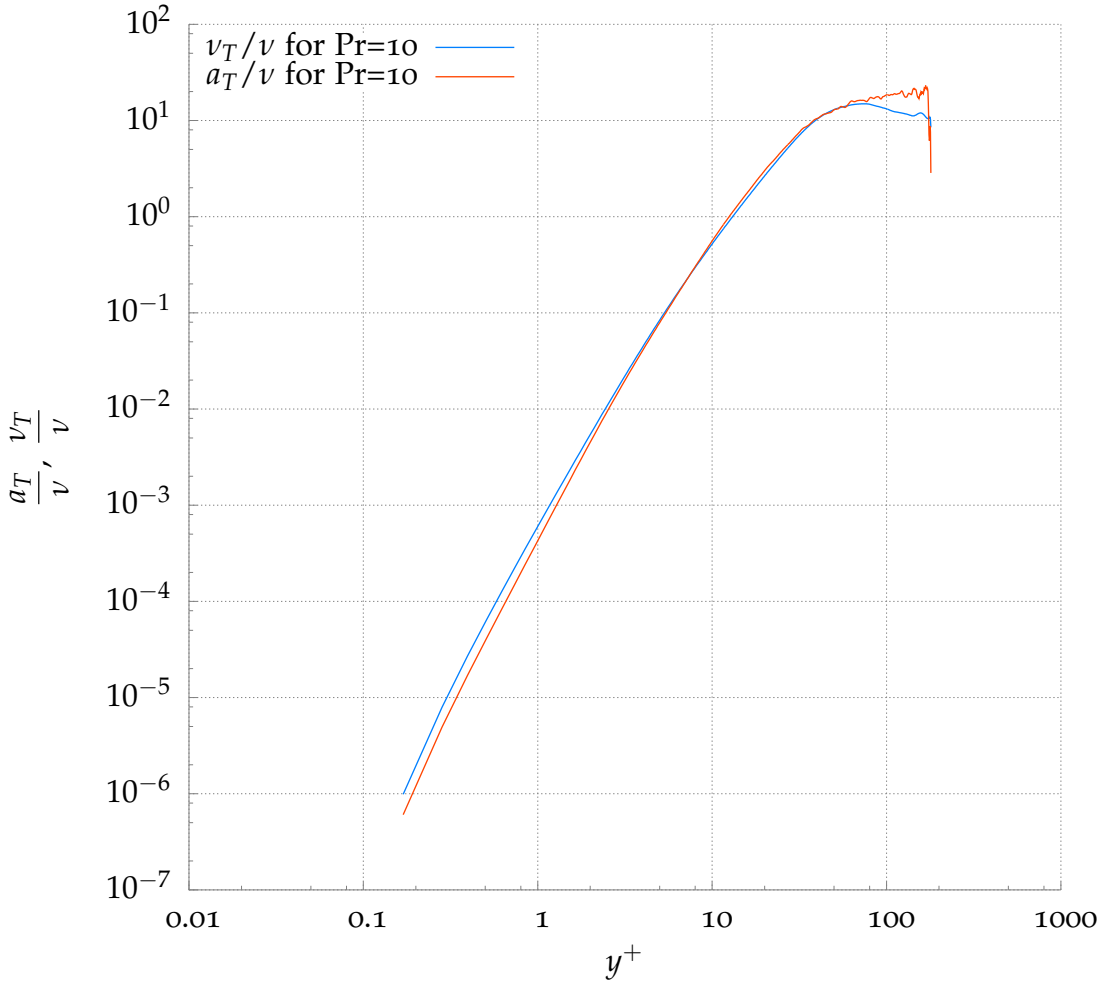

Figure 4.13: Near wall variation of the eddy viscosity and conductivity for $Pr = 10$.

In comparison to the evaluation of eq. (4.5) based on DNS data, an evaluation with experimental data is very difficult, as the input quantities on the right-hand side are very hard to measure close to the wall. Owing to this fact there are hardly any experimental data available on the near wall variation of the turbulent Prandtl number. Hollingsworth et al. (1989) performed measurements for a fully turbulent boundary layer in a free-surface channel flow with zero pressure gradient and $Pr = 5.9$. Figure 4.15 shows the variation of Pr_T obtained from the DNS results for $Pr = 5.9$ (by evaluating

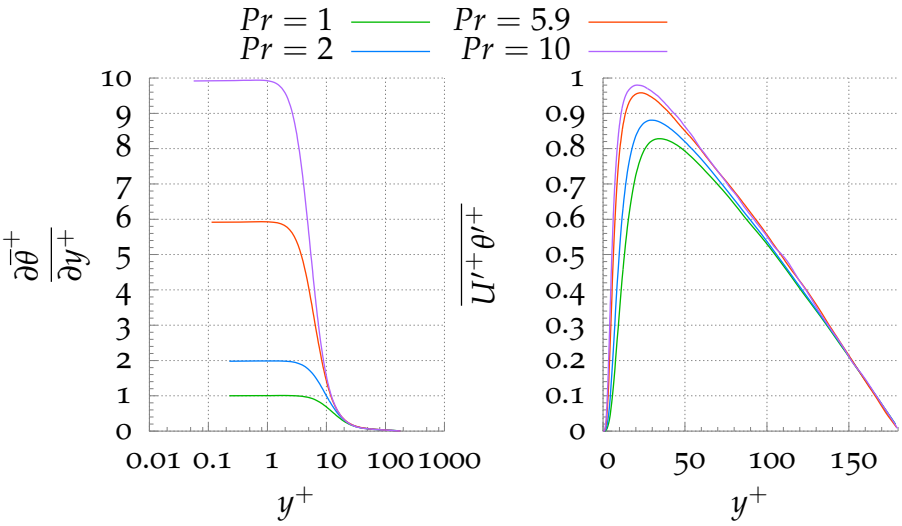

Figure 4.14: Variation of the temperature gradient and turbulent heat flux for different Pr.

eq. (4.5)) plotted together with the experimental data of Hollingsworth et al. (1989), although their investigated flow configuration differs considerably from the simulated pipe flow. Roughly speaking, both profiles exhibit the same tendency. Pr_T starts from a rather small value around $Pr_T \approx 0.5$ in the wall remote region, oscillates around unity in the inertial region, and increases in the region of transition to the viscous sublayer near the wall. The quantitative increase of Pr_T near the wall is still much higher in the experiments, which may be due to the different flow configurations.

Empirical correlation for Pr_T

Kays and Crawford (1993) proposed a mathematical model for the turbulent Prandtl number, which is based on measurement data of a pipe flow at high Reynold number. The correlation is written as

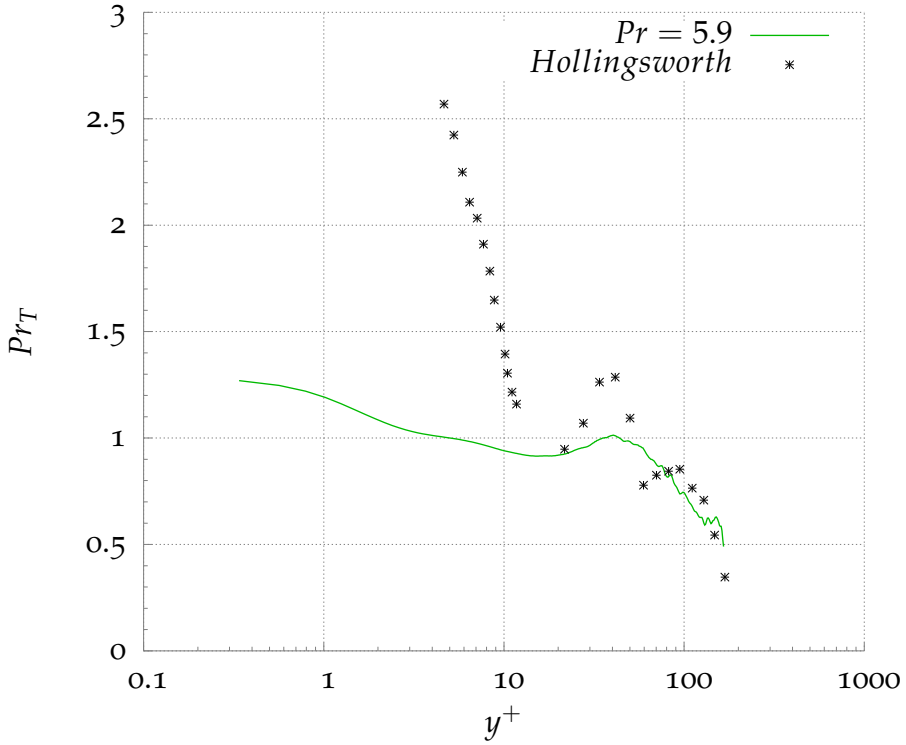

Figure 4.15: Pr_T obtained from the DNS data and the measurements done by Hollingsworth et al. (1989).

$$Pr_T = \frac{1}{\frac{1}{2Pr_{T\infty}} + CPe_T\sqrt{\frac{1}{Pr_{T\infty}}} - (CPe_T)^2\left[1 - e^{\left(-\frac{1}{CPe_T\sqrt{Pr_{T\infty}}}\right)}\right]}, \tag{4.6}$$

where Pe_T is the turbulent Peclet number, and C is an experimental model constant, for which Kays and Crawford (1993) proposed $C = 0.3$. The dependence on the distance to the wall is incorporated in terms of the turbulent Peclet number, defined as

$$Pe_T = \frac{\nu_T}{\nu} Pr. \tag{4.7}$$

As the viscosity ratio scales with

$$\frac{\nu_T}{\nu} \sim y^+$$

Pe_T varies from zero at the wall to infinity in the core region remote from the wall. The correlation (4.6) was basically developed for small molecular Prandtl numbers $Pr < 1$, but the authors claim that the correlation is applicable to Prandtl numbers $Pr > 1$ up to $Pr \approx 6$ (e.g., water), provided that the Peclet number is always computed with $Pr = 0.7$. This suggests that results obtained for $Pr = 0.7$ (e.g. for air) can be directly used for Prandtl numbers of liquids up to about $Pr = 6$. Figure 4.16 compares the variation of Pr_T obtained from the present DNS results against the correlation of Kays and Crawford (1993). As outlined above the latter is always the same curve for the considered Prandtl numbers $Pr = 1, 2, 5.9$, and 10, where the turbulent Peclet number was computed as

$$Pe_T = \kappa y^+ 0.7 \tag{4.8}$$

and the asymptotic limit for $y^+ \to \infty$ was set to $Pr_{T\,\infty} = 0.85$. Based on these inputs the curve obtained from eq. (4.6) varies between $Pr_T = 2Pr_{T\,\infty} = 1.7$ at $y^+ = 0$ and $Pr_T = Pr_{T\,\infty} = 0.85$ for $y^+ \to \infty$.

It is interesting to see the best agreement between the DNS data and the model correlation is observed for the highest molecular Prandtl number $Pr = 10$, while significant deviations appear in the near wall region for all other cases. The inherently imposed independence of the molecular Prandtl number by substituting always $Pr = 0.7$ into eq. (4.6) is evidently not confirmed by the results of the DNS.

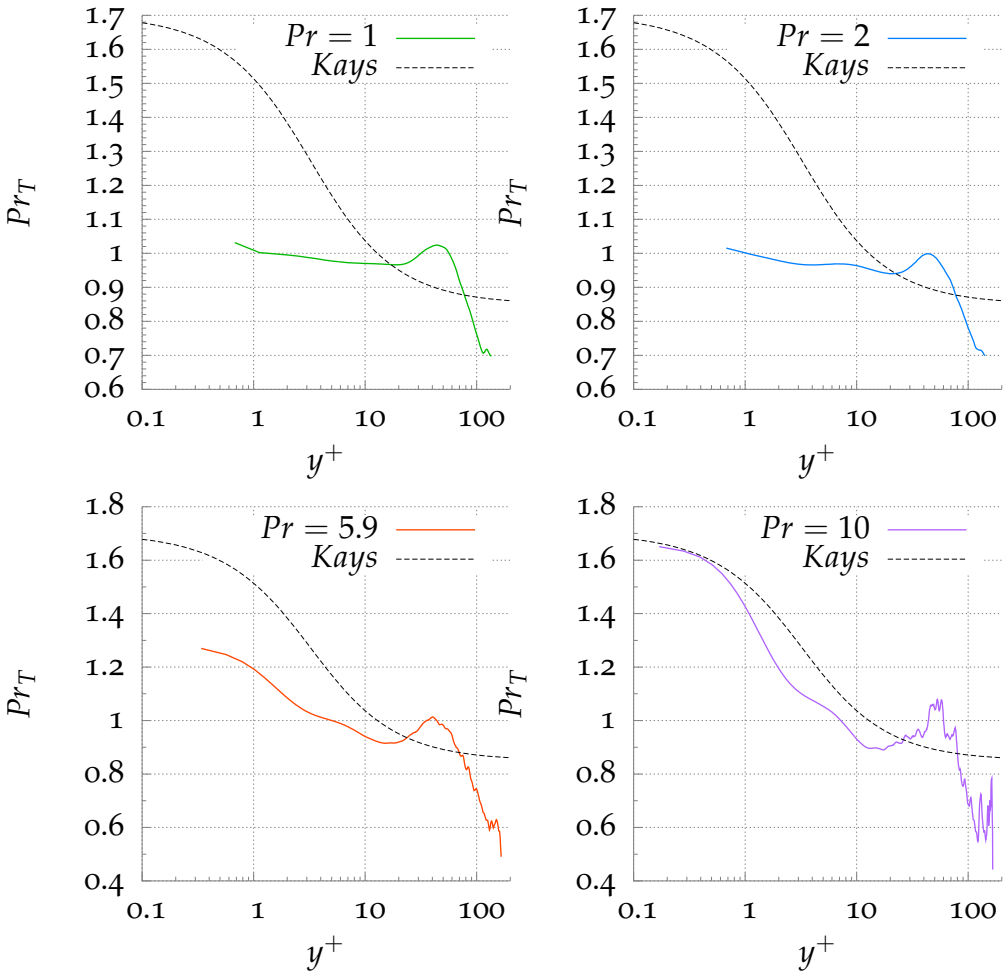

Figure 4.16: DNS results for Pr_T compared against Pr_T model of Kays and Crawford (1993).

4.3.1.4 P-function

The reliability of the thermal log-law given by equation (2.57) for describing the turbulent heat transfer strongly depends on the appropriate setting of the parameters κ_θ and β_θ.

Based on the DNS data it is possible to compute the variation of these two parameters along the non-dimensional wall distance y^+ by evaluating

the following expressions:

$$\kappa_\theta = \frac{1}{y^+} \left(\frac{\partial \overline{\theta}^+}{\partial y^+} \right)^{-1} \tag{4.9}$$

$$\beta_\theta = \overline{\theta}^+ - \kappa_\theta ln\left(y^+\right) \tag{4.10}$$

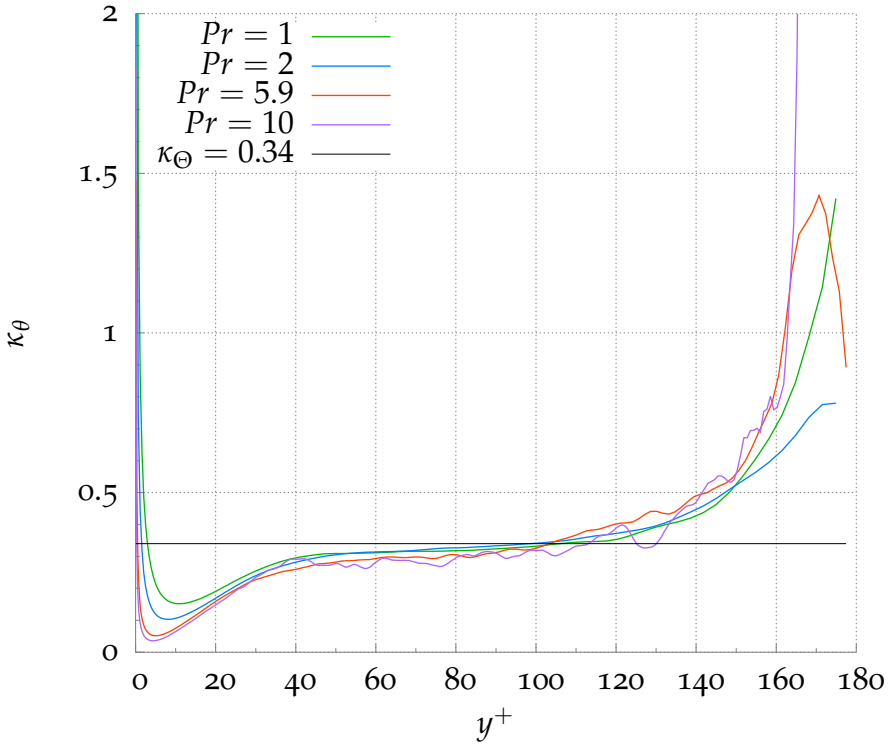

Figure 4.17: Variation of κ_θ in the radial direction.

As seen from the resulting variations for κ_θ in figure 4.17, a plateau around $\kappa_\theta = 0.34$ can be identified in the inertial sublayer. This level is somewhat smaller than the value obtained by Kawamura et al. (1999) for a channel flow being $\kappa_\theta = 0.4$. κ_θ basically represents the ratio

$$\kappa_\theta = \frac{\kappa}{Pr_T}. \tag{4.11}$$

Substituting into this expression the value for the von Kármán constant $\kappa = 0.34$ computed from the present DNS results using eq. (4.1), the turbulent Prandtl number becomes

$$Pr_T = \frac{\kappa}{\kappa_\theta} = 1.00. \tag{4.12}$$

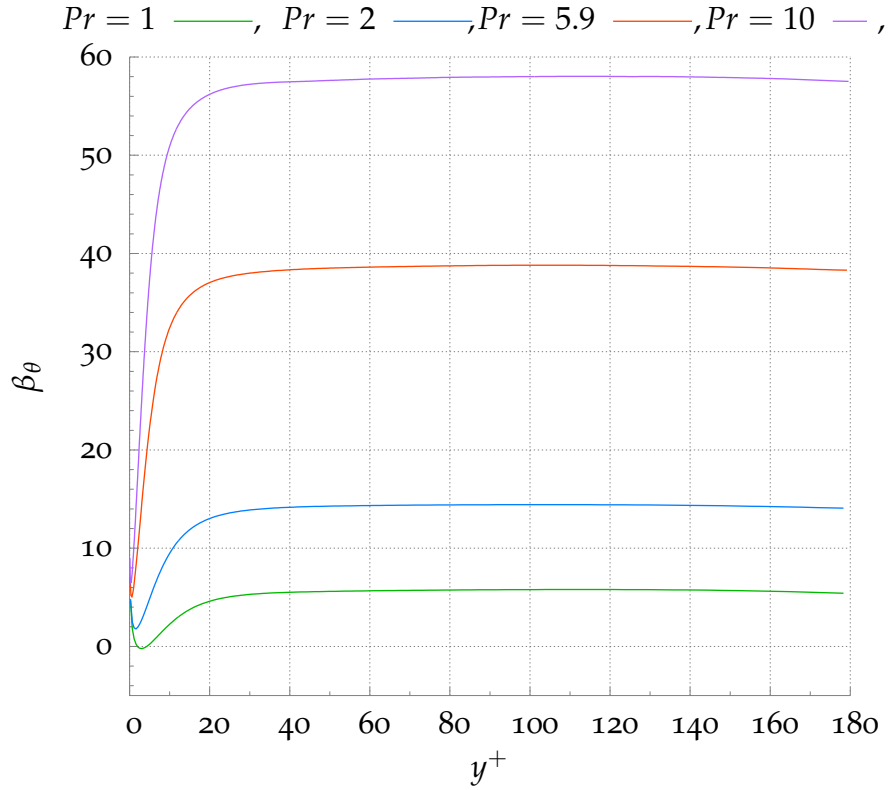

Figure 4.18: Variation of β_θ in the radial direction.

The results obtained for β_θ by evaluating eq. (4.10) using κ_θ from eq. (4.9) are shown in Figure 4.18. β_θ strongly decreases to a local minimum close to

the wall. Aside from that it approaches an almost constant level for the most part of the inertial region beyond $y^+ > 20$. Thereby, β_θ reaches markedly higher constant levels for increasing molecular Prandtl numbers.

Combining the log-laws for the velocity and the temperature given by equations (2.45) and (2.58), respectively, the temperature can be rewritten as

$$\overline{\theta}^+ = Pr_T(\overline{W}^+ + P). \tag{4.13}$$

This implies that the logarithmic temperature profile can be computed directly from the logarithmic velocity profile including an additive term P, known as P-function. The P-function basically represents the thermal resistance of the viscous sublayer, so that it strongly depends on the molecular Prandtl number. It is related to the parameter β_θ by

$$P = \frac{\beta_\theta}{Pr_T} - \beta \tag{4.14}$$

involving the integration constant β from equation (2.45).

Various analytical, semi-empirical, and fully empirical correlations have been proposed for the P-function. The most popular one was introduced by Jayatilleke (1969), who essentially extended the analytically derived correlation of Spalding (1967) by incorporating an empirically based modification. Both correlations shall be described in more detail and validated against the present DNS results below.

Spalding P-function

Spalding (1967) derived analytically an expression for the P-function in the limit of high Prandtl numbers. Owing to this assumption, the thermal

boundary thickness is very small compared to the thickness of the velocity boundary layer. Therefore, it is possible to use the viscous velocity profile ($\overline{W}^+ = y^+$) for the whole thermal boundary layer, which is substituted into the viscosity ratio computed from

$$\frac{\nu_T}{\nu} = (\kappa y^+) \left[1 - e^{\frac{-y^+}{A^+}} \right] \frac{\partial \overline{W}^+}{\partial y^+} \tag{4.15}$$

involving the van Driest wall damping function with $A^+ = 26$. The P-function derived by Spalding finally reads

$$P^{Spalding} = \left(\frac{Pr}{Pr_T} - 1 \right) \left(\frac{Pr}{Pr_T} \right)^{-1/4} \frac{\pi}{4sin(\pi/4)} \left(\frac{A^+}{\kappa} \right)^{0.5}, \tag{4.16}$$

where the turbulent Prandtl number is mostly set to a constant value $Pr_T = 0.9$.

Jayatilleke P-function

Jayatilleke (1969) published a modified P-function based on Spalding's approach, which reads

$$P = 9.24 \left[\left(\frac{Pr}{Pr_T} \right)^{3/4} - 1 \right] \left[1 + 0.28 e^{\left(-0.007 \frac{Pr}{Pr_T} \right)} \right], \tag{4.17}$$

where the last square-bracketed term represents an empirically based function for modification.

Jayatilleke suggested to use the constant value $Pr_T = 0.9$.

The P-function proposed by Spalding and Jayatilleke using both $Pr_T = 0.9$ are plotted over the molecular Prandtl number in Figure 4.19. The curves evidently coincide for very high Prandtl numbers.

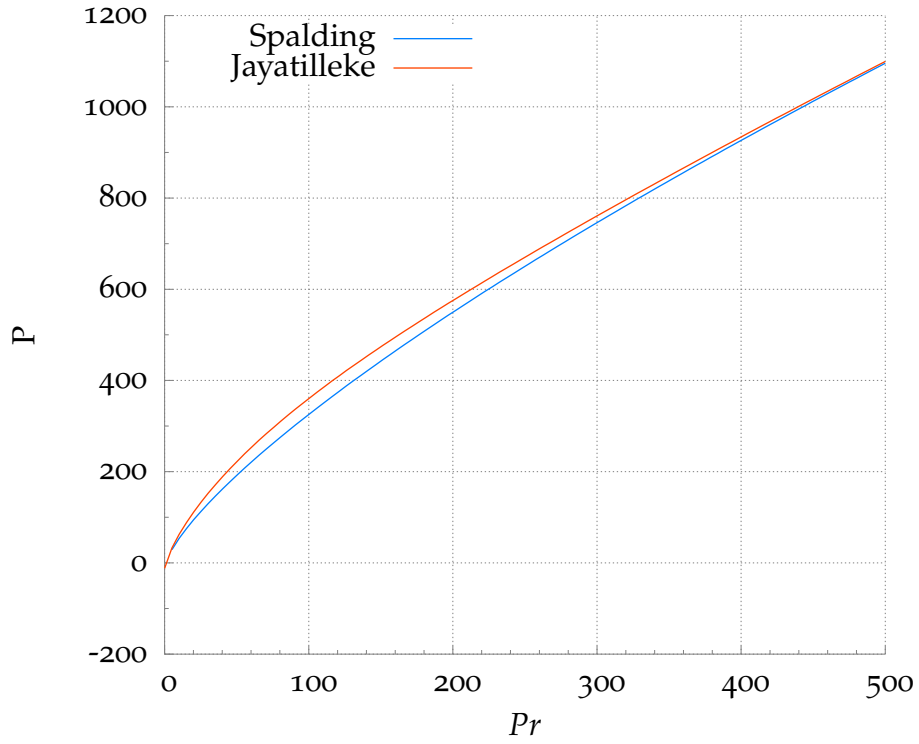

Figure 4.19: P-function of Spalding and Jayatilleke vs. Pr.

Validation against DNS results

The correlations for the P-function proposed by Spalding and Jayatilleke are validated against the DNS results based on equation (4.13). For this purpose equation (4.13) is rewritten as

$$P = \frac{\overline{\theta}^+}{Pr_T} - \overline{W}^+ \tag{4.18}$$

and evaluated at selected positions ($y^+ = 20, 25, 30, 35$) substituting the local DNS results for $\overline{W}^+$, $\overline{\theta}^+$ and Pr_T, whose profiles were already shown in Figures 4.1, 4.7, and 4.11, respectively. The local turbulent Prandtl numbers used as input into this evaluation are listed in table 4.2 for the different molecular Prandtl numbers.

	Pr_T			
Pr	$y^+ = 20$	$y^+ = 25$	$y^+ = 30$	$y^+ = 35$
1	0.967	0.975	0.994	1.012
2	0.940	0.944	0.960	0.981
5.9	0.916	0.936	0.959	0.987
10	0.882	0.908	0.929	0.967

Table 4.2: Turbulent Prandtl numbers obtained from DNS results at selected positions.

Figure 4.20 shows the results obtained from the evaluation of equation (4.18) compared against the prediction of the correlations of Spalding and Jayatilleke for varying molecular Prandtl numbers. The Jayatilleke P-function agrees evidently fairly well with the DNS results, although the scatter dependent of the individual y^+-position is increasing for increasing Prandtl numbers. The observed scatter can be attributed to the stronger variation of the turbulent Prandtl number Pr_T with y^+ for the higher molecular Prandtl numbers, as seen in table 4.2.

Analogously to the computation of the P-function by evaluating eq. (4.18) with DNS data the integration constant β_θ is computed by rewriting the log-law for the temperature, eq. (2.58), as

$$\beta_\theta = \overline{\theta}^+ - \frac{1}{\kappa_\theta} ln(y^+) \tag{4.19}$$

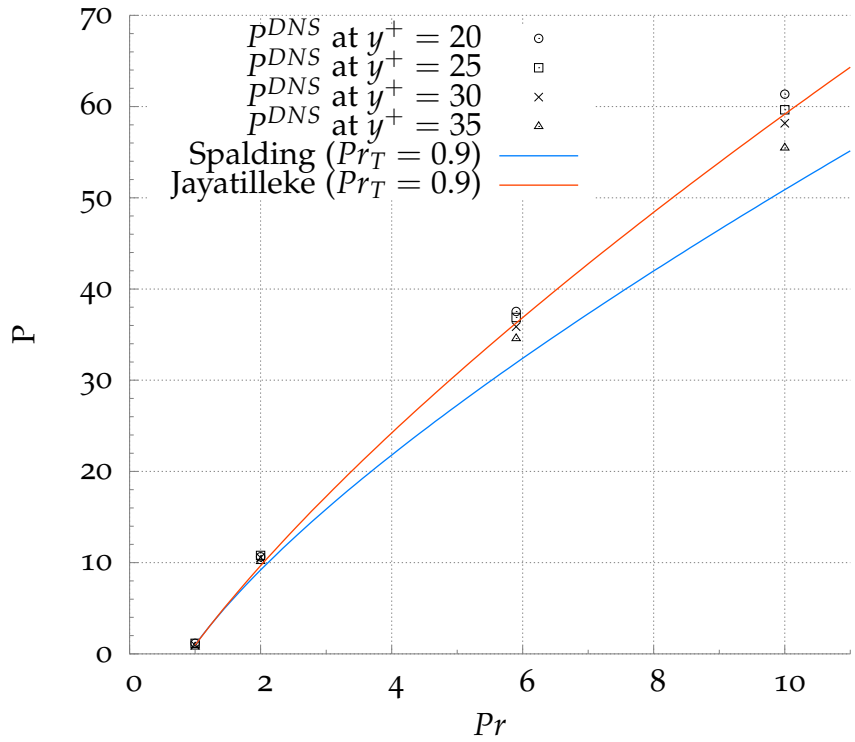

Figure 4.20: P-functions compared against DNS results.

and evaluating it with DNS data at the positions $y^+ = 20, 25, 30, 35$. Figure 4.21 shows the obtained results plotted together with the variations of β_θ, which correspond to the P-functions of Spalding and Jayatilleke computed from the relation

$$\beta_\theta = P + Pr_T\beta \tag{4.20}$$

using the correlations (4.16) and (4.17) for P, with Pr_T and β set to 0.9 and 5.5, respectively.

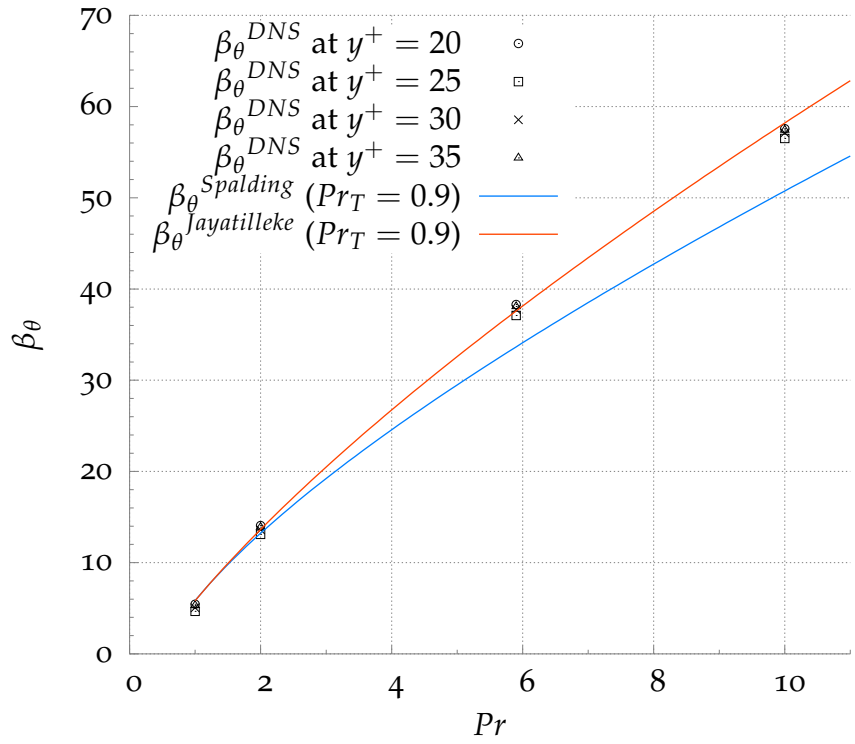

Figure 4.21: β_θ obtained from DNS results compared against β_θ obtained from P-functions of Spalding and Jayatilleke.

The agreement of β_θ based on the Jayatilleke P-function with the DNS results is very good, which basically reflects the validation of the P-function itself shown in Figure 4.20, as one might expect. Moreover, there is considerably less scatter in the DNS based results for β_θ than in those obtained for P. This indicates that the parameter β_θ is evidently less sensitive to the increased spatial variation of the turbulent Prandtl number occurring at higher molecular Prandtl numbers. From this point of view it appears to be as favourable to compute the temperature $\overline{\theta}^+$ directly from the log-law, eq. (2.58), with an appropriate model for $\beta_\theta = \beta_\theta(Pr)$ instead of using eq. (4.13) with a model for the P-function. β_θ needs thereby not to be modelled separately but can rather simply computed from the relation (4.20) using the Jayatilleke P-function, such that $\beta_\theta = \beta_\theta{}^{Jayatilleke}$.

Due to the good agreement between ${\beta_\theta}^{Jayatilleke}$ and the DNS results observed in Figure 4.21 one would expect a good agreement with the log-law for the temperature, eq. (2.58) evaluated with $\beta_\theta = {\beta_\theta}^{Jayatilleke}$, as well.

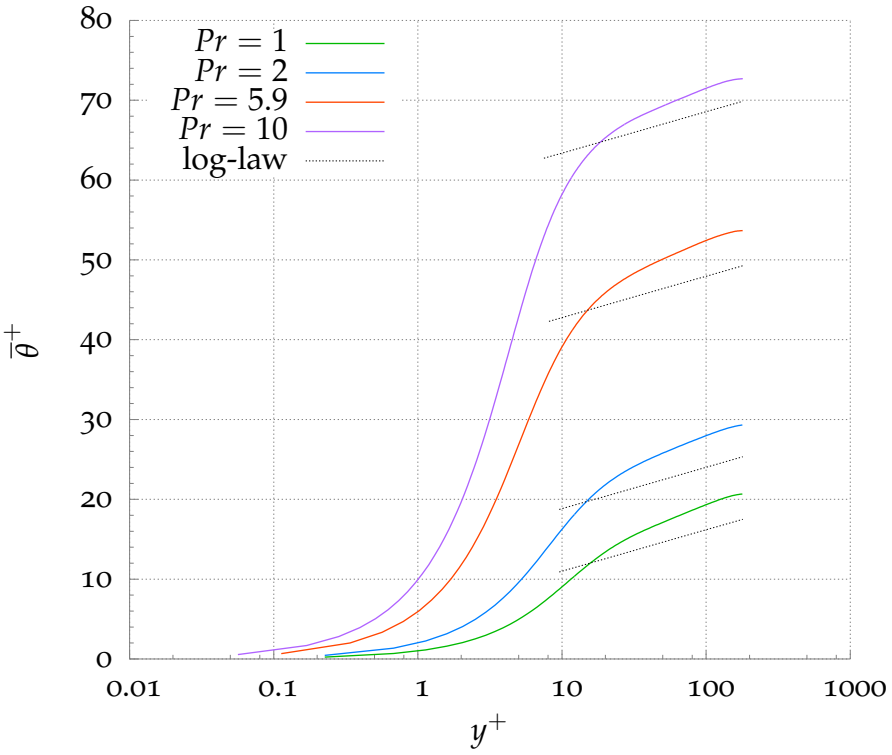

Figure 4.22: Log-law for the temperature using $\kappa_\theta = \dfrac{\kappa}{Pr_T} = \dfrac{0.4}{0.9}$ and ${\beta_\theta}^{Jayatilleke}$ compared against DNS results.

However, as seen from Figure 4.22, there still appear considerable discrepancies between the log-law and the DNS results in the inertial sublayer. Given the good agreement seen for β_θ the observed deviations have to be attributed to the parameter κ_θ. In the shown log-law this parameter is computed from

$$\kappa_\theta = \frac{\kappa}{Pr_T}$$

using the standard input parameter $\kappa = 0.4$ and $Pr_T = 0.9$ as suggested by Kays and Crawford (1993).

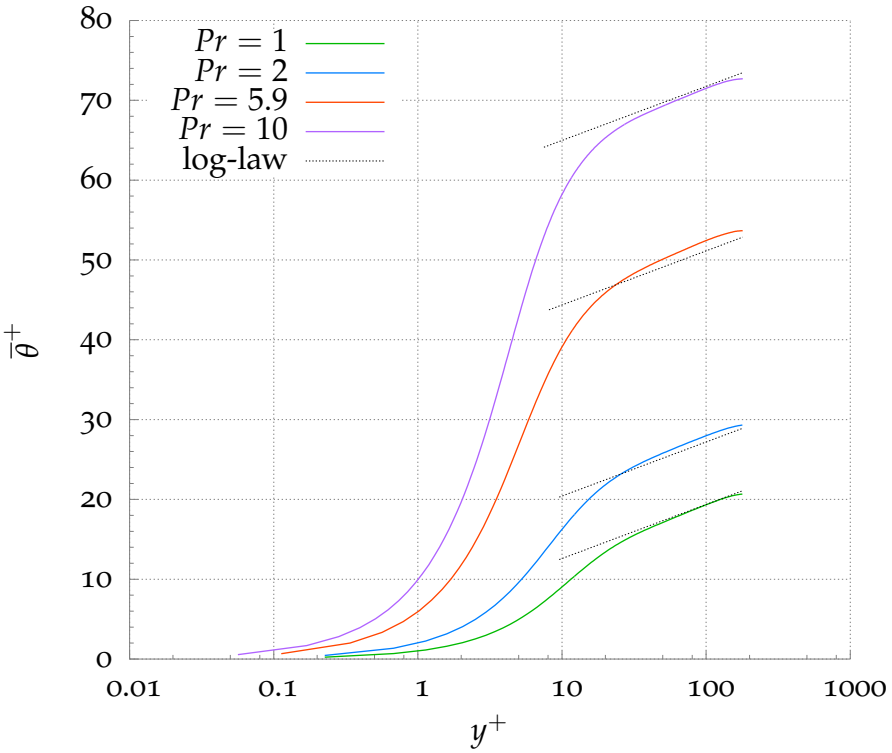

Figure 4.23: Log-law for the temperature using $\kappa_\theta = 0.34$ and $\beta_\theta{}^{Jayatilleke}$ compared against DNS results.

Setting instead the parameter κ_θ to the value $\kappa_\theta = 0.34$, which was extracted from the DNS results as a reliable general mean value in the inertial subrange for all considered Prandtl numbers, significantly improves the agreement with the log-law. This is clearly seen in Figure 4.23 comparing the log-laws, eq. (2.58), evaluated with $\kappa = 0.34$ and $\beta_\theta = \beta_\theta{}^{Jayatilleke}$, against the DNS results.

Due to the dependency of the parameter κ_θ of Pr_T, as it follows from eq. (4.11), it can be concluded that the appropriate modelling of the turbulent Prandtl number is by far more important than the modelling of the P-function.

4.3.2 Nusselt number

Based on the solution for the temperature the Nusselt number is computed as follows:

$$Nu = \frac{\alpha D}{\lambda} = \frac{q_w}{T_w - \overline{T}_m} \cdot \frac{D}{\lambda}$$

Recalling

$$\overline{\theta}^+ = \frac{T_w - \overline{T}}{q_w} \rho c w_\tau$$

we obtain

$$\overline{\theta}_m^+ = \frac{T_w - \overline{T}_m}{q_w} \rho c w_\tau = \frac{\int_{A^*} \overline{W}^+ \overline{\theta}^+ \mathrm{d}A^*}{\overline{w}_m^+ A^*}$$

so that

$$Nu = \frac{w_\tau}{\overline{\theta}_m^+} \cdot \frac{\rho c D}{\lambda}, \tag{4.21}$$

which can be rewritten as

$$Nu = \frac{Re_\tau Pr}{\overline{\theta}_m^+}. \tag{4.22}$$

The following table shows the Nusselt number obtained from equation (4.22) based on the DNS data:

Pr	Nu
1	21.044
2	28.132
5.9	42.792
10	52.392

It was possible to fit a curve to the DNS data by using the method of least squares ($R^2 = 0.9999$) yielding the following correlation:

$$Nu = 3.842ln(Re_D)^{0.796}Pr^{0.392} \tag{4.23}$$

There are many well established correlations available to be compared against the present results for the Nusselt number. Gnielinski (1975) published a correlation which computes the Nusselt number dependent of the wall friction coefficient and is written as

$$Nu = \frac{c_f/2(Re_D - 1000)Pr}{1 + 12.7\sqrt{c_f/2}\left(Pr^{2/3} - 1\right)}. \tag{4.24}$$

Therein, the friction coefficient is obtained from the correlation developed by Petukhov et al. (1973) already shown by eq. (4.3). Owing to the fact that the correlation of Petukhov et al. (1973) varies with the logarithm of Re_D the curve-fit of the present DNS results given by eq. (4.23) was also assumed as dependent of the logarithm of Re_D.

Figure 4.24 shows the Nusselt numbers obtained from the DNS together with the curve-fit given by eq. (4.23) compared against the predictions of the correlations of Gnielinski and Dittus-Boelter (see eq. (2.82)). The discrepancies evidently tend to increase for the higher Prandtl numbers. The predictions of the Dittus-Boelter correlation exhibits larger deviations from

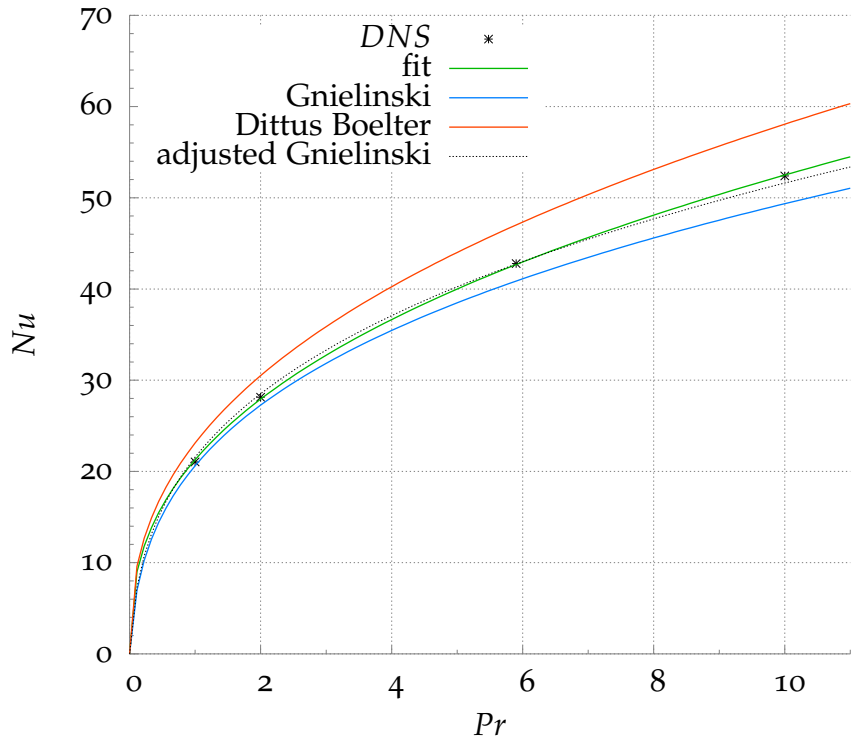

Figure 4.24: Nu obtained from the DNS compared against popular correlations.

the DNS data. This may be attributed to the fact that the Dittus-Boelter equation is basically deviced for higher Reynolds number turbulent flow. In the presently considered flow the bulk Reynolds number $Re = 5300$ is fairly low, but still high enough to be in the turbulent regime.
The Nu correlation according to Gnielinski (1975) agrees better with the DNS data, but it still shows some offset throughout the entire Prandtl number range to a lower value.

This offset is associated with the constant reduction of the Reynolds number occurring in the correlation eq. (4.24). Gnielinski introduced this reduction of the Reynolds number by 1000 to account for the reduced turbulent heat transfer at low Reynolds numbers near the critical limit $Re_{crit} = 2300$. Modifying this constant reduction from 1000 to 800 already leads to significantly improved agreement with the DNS data, as seen from the dashed line in

Figure 4.24, which was obtained with this modification.

4.3.3 Computation time

As already mentioned, the computational grid was refined with increasing Prandtl number, which resulted in an increasing computation time. Due to the CFL criterion the computation time does not increase on a linear scale, which is shown in figure 4.25.

Each simulation was performed over a non-dimensional time-span

$$\Delta t^* = \frac{w_\tau \Delta t}{D} = 5,$$

which is equivalent to 15 flow-through times.

Pr	number of grid cells	computational time	time step Δt^*
–	–	*days*	–
1	8192000	3.63	0.0000870
2	8192000	3.63	0.0000870
5.9	16384000	27.17	0.0000255
10	32768000	230.43	0.0000066

Table 4.3: Computational parameters for the different Prandtl number cases.

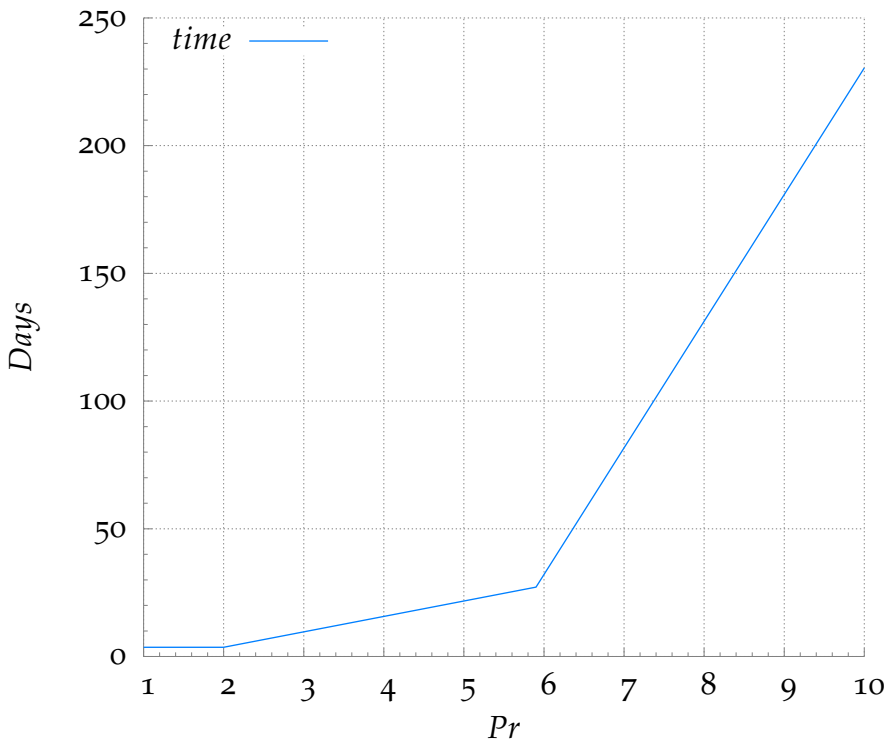

Figure 4.25: Computation time for the different Prandtl number cases.

5 Summary and Conclusions

The present work performed Direct Numerical Simulation (DNS) of heated turbulent pipe flow. Based on the DNS results obtained for molecular Prandtl numbers varying from $Pr = 1$ to $Pr = 10$ the study examined in particular the applicability of the most essential assumptions generally made for the wall-function based modelling of the thermal boundary conditions, which is widely applied in $RANS$-type simulations.

The DNS results of the flow field showed a very good agreement with experimental data from literature. Inside the inertial sublayer the DNS data somewhat deviated from the log-law profiles evaluated with the standard value for the von Kármán constant being $\kappa = 0.4$. These deviations decrease with increasing Reynolds numbers, as it was shown by DNS carried out for higher Reynolds numbers. The here observed tendency is well consistent with experimental findings.

The analysis of the DNS results for the temperature and the turbulent heat fluxes provided a detailed insight into the near-wall variation of the turbulent Prandtl number Pr_T. In the inertial sublayer Pr_T remains constant around unity for all considered molecular Prandtl numbers. With this respect the DNS results confirm a major assumption commonly made in the wall-function based modelling, although Pr_T is generally set to a constant value a little bit smaller than unity $Pr_T = 0.9$. The assumption of a constant turbulent Prandtl number breaks down for the higher molecular Prandtl numbers when approaching the viscous sublayer, where the DNS results exhibit a considerable increase of Pr_T towards the wall. A popular correlation proposed for Pr_T by Kays and Crawford (1993) is not capable to describe this Pr-dependent effect.

The validation of the P-function based wall modelling of the thermal boundary conditions gave the following results:

The P-function proposed by Jayatilleke (1969) showed a good agreement with the corresponding values for P obtained from the DNS data. This

was not the case for the P-function of Spalding (1967), where significant deviations from the DNS data appeared at the higher Pr numbers.
The comparison of the DNS results for the temperature against the log-law emphasized the importance of an appropriate setting of the parameter κ_θ, which basically determines the linear increase of the thermal mixing length according to $l^+_{m\theta} = \kappa_\theta y^+$. It is shown by the DNS results that this parameter remains approximately constant in the inertial sublayer for all considered Pr numbers being about $\kappa_\theta = 0.34$. Substituting this value into the log-law for the temperature improves significantly the agreement with the DNS results as compared to the log-law evaluated with the widely used standard setting $\kappa_\theta = \frac{\kappa}{Pr_T}$ with $\kappa = 0.4$ and $Pr_T = 0.9$. Thus, for the considered range of Pr numbers the assumption of a constant parameter κ_θ appears as justified provided that the considered region is inside the inertial sublayer and κ_θ is set to an appropriate value.

The comparison of the Nusselt numbers predicted by the DNS against popular empirical correlations showed a fairly good agreement with the correlation proposed by Gnielinski (1975). The observed agreement could even be improved by applying a minor modification to a model parameter which was introduced by Gnielinski to cover the low Reynolds number range as well.

Appendix

Bibliography

Antonia, R. A. and J. Kim (1991). "Turbulent Prandtl number in the near-wall region of a turbulent channel flow". In: *International Journal of Heat and Fluid Flow* 34, pp. 1905–1908 (cit. on p. 2).

Brenn, G. and W. Meile (2009). *Strömungslehre und Wärmeübertragung*. lecture notes (cit. on p. 32).

Coles, D. (1956). "The law of the wake in the turbulent boundary layer". In: *Coles* 1, pp. 191–226 (cit. on p. 23).

Durst, F., M. Fischer, J. Jovanovic, and H. Kikura (1998). "Methods to Set Up and Investigate Low Reynolds Number, Fully Developed Turbulent Plane Channel Flows." In: *Journal of Fluids Engineering* 120, pp. 496–503 (cit. on pp. 53, 54).

Durst, F., J. Jovanovic, and J. Sender (1995). "LDA measurements in near-wall region of a turbulent pipe flow". In: *Journal of Fluid Mechanics* 295, pp. 305–335 (cit. on p. 53).

Gnielinski, V. (1975). "Neue Gleichungen für den Waerme- und den Stoffuebergang in turbulent durchstroemten Rohren und Kanaelen". In: *Forschung im Ingenieurwesen* 41 (1), pp. 8–16 (cit. on pp. 81, 82, 86).

Hirsch, C. (1988). *Numerical Computation of Internal and External Flows, Volume 1*. JOHN WILEY and SONS (cit. on p. 47).

Hollingsworth, D. K., W. M. Kays, and R. J. Moffat (Aug. 1989). "The measurement and prediction of heat transfer in a turbulent boundary layer in water". In: *Symposium on Turbulent Shear Flows*. Vol. 2. 7th. Stanford, CA (cit. on pp. 3, 65–67).

Jayatilleke, C. L. V. (1969). "The influence of Prandtl number and surface roughness on the resistance of the laminar sublayer to momentum and heat transfer". In: *Progress in heat and mass transfer* 1, pp. 193–321 (cit. on pp. v, 72, 73, 85).

Kawamura, H., H. Abe, and Y. Matsuo (1999). "DNS of turbulent heat transfer in channel low with respect to Reynolds and Prandtl number effects". In: *International Journal of Heat and Fluid Flow* 20, pp. 196–207 (cit. on pp. 2, 60, 70).

Kays, W. M. and M. E. Crawford (1993). *Convective heat and mass tansfer*. 3rd. McGraw-Hill (cit. on pp. 2, 19, 24, 51, 52, 66–69, 79, 85).

Kim, J. and P. Moin (Sept. 1987). "Transport of Passive Scalars in Turbulent Channel Flow". In: 89463 (cit. on p. 2).

Oertel, H. (2002). *Prandtl -Führer duch die Stömungslehre*. 11rd. Vieweg (cit. on pp. 16, 20).

Ould-Rouiss, M., M. Bousbai, and A. Mazouz (2013). "Large-Eddy simulation of turbulent heat transfer in pipe flows with respect to Reynolds and Prandtl number effects." In: *Acta Mechanica* 224, pp. 1133–1155 (cit. on p. 3).

Petukhov, B. S., V. A. Kurganov, and A. I. Gladuntsov (1973). "Heat transfer in turbulent pipe flow of gases with variable properties." In: *Heat Transfer-Soviet Research* 5, pp. 109–116 (cit. on pp. 55, 81).

Pope, S. B. (2000). *Turbulent flow*. Cambridge University Press (cit. on p. 12).

Spalding, D. B. (1967). "Monograph on turbulent boundary layers." In: Imperial College Mechanical Engineering Department. Chap. Chapter 2 (cit. on pp. 72, 86).

Tennekes, H. and J. L. Lumley (1972). *A first course in turbulence*. MIT Press (cit. on pp. 17, 51).

van Driest, E.R. (1956). "On turbulent flows Near a wall". In: *Journal of the Aeronautical Sciences* 23, pp. 1007–1011 (cit. on p. 20).